UNIVERSITY OF SOUTHERN QUEENSLAND

The Active Young Solar-Type Star HR 1817 (= HD 35850)

A dissertation submitted by

Matthew Wayne Mengel

B.IT, Grad.Dip.IT

For the Award of

Master of Philosophy

Department of Biological and Physical Sciences

University of Southern Queensland

August 2005

Abstract

The active F dwarf HR 1817 represents the upper temperature extreme of what are broadly termed solar-type stars – stars which have the same internal structure as the Sun, albeit in this case with a much smaller convective zone. To date, studies of the active surface features and magnetic fields of solar-type stars have been restricted to G and K dwarfs. This thesis investigates the surface and magnetic features of HR 1817 using the techniques of Doppler and Zeeman Doppler Imaging, resulting in tomographic maps of the stellar surface and magnetic field.

Cooler stars than HR 1817 exhibit large polar spots, and while HR 1817 also exhibits a polar spot, it is not nearly as large as those usually seen. The lower-latitude surface features of HR 1817 are weak but well defined and cover a relatively small area of the stellar surface. Total spot coverage is relatively small (~ 1.7 - 2%).

Zeeman Doppler Imaging reveals that HR 1817 exhibits a richly-detailed, though weak magnetic topography. A ring of azimuthal field appears around the pole, while the radial field exhibits many well-defined and distinct bipolar mid-latitude magnetic features, perhaps indicating a more dominant interface dynamo as opposed to the posited distributed dynamo of cooler active dwarfs.

Finally, a differential rotation measurement of the star indicates an extremely large rotational shear. Values for the equatorial rotation (Ω_{eq}) and rotational shear ($d\Omega$) of 6.494 ± 0.010 rad/d and 0.256 ± 0.017 rad/d respectively are found. This Ω_{eq} is equivalent to a rotational period for HR 1817 of ~ 0.98 days. The very high rotational shear of 0.256 rad/d is fast enough for the equator to lap the pole in approximately 23 days.

Certification of Dissertation

I certify that this dissertation contains no material accepted for the award of any other degree or diploma in any university. To the best of my knowledge, it contains no material published or written by another person, except where due reference is made in the text.

Signature of Candidate | Date

ENDORSEMENT

Signature of Supervisor | Date

Acknowledgements

The road to completing this thesis has been long and difficult for me, especially while working a demanding job more than full-time in the University's IT Department. I would like to thank my principal supervisor Brad Carter for staying the course with me and being so supportive and understanding when work and illness have meant that I couldn't give this thesis the attention it needed and deserved.

Enormous thanks also to my associate supervisor Stephen Marsden for all his assistance and advice. The quality of the analysis and output has been immeasurably improved by his input.

I would like to also thank Jean-François Donati for his assistance, and for allowing me the use of the ESpRIT code. Thanks as well for Meir Semel for the use of the polarimeter at the AAT. Pascal Petit also provided assistance in getting some of the prettier maps out using my ancient code base.

This work could not have been possible without the excellent work by all at the AAT, including the operators, duty astronomers, technical staff and administrative staff.

Thanks go to Ruth Hilton and all in the USQ Research and Higher Degrees office. I have tested their patience in getting this all done, but they have stuck by me and given me assistance without which it would have been so easy to give up. Also, to my supervisors and colleagues in the Information Technology Services department at USQ, thanks for doing what you could when I needed to get away to observe, or to get this thing written.

Finally, thanks to my family for helping me along. And in answer to your constant questions, yes, it is finished now!

Contents

List of Figures

List of Tables

Chapter 1

Introduction

The Earth's nearest stellar neighbour in space is the Sun. A typical G2 dwarf star, the Sun is the only dwarf star whose surface can be resolved directly. Hence the Sun is an archetype for studies with much to tell us about similar stars. However, this solar-stellar connection is a reciprocal arrangement in that the study of other dwarf stars can also give us insights into the activity of the Sun. Observations of G and K dwarfs using different techniques have shown that the Sun is not alone in exhibiting phenomena indicating an active atmosphere such as spots and flares (Schrijver and Zwann, 2000).

While the Sun has been extensively studied, these studies have been over a very short period; a tiny fraction of the Sun's life. This means that all we have is a mere snapshot of the Sun as it is now. This is useful in itself, however the study of different stars at differing ages, masses, temperatures and levels of activity allows us to not only investigate the continuum of dwarf star activity and the Sun's place in it, but we may also

be able to infer the evolution of the Sun and in particular its early history (Baliunas, 1991).

1.1 The Sun

The Sun is a main-sequence G2V dwarf star which is approximately 4.5 x 10^9 years old. Due to the proximity of the Sun, it is the star about which we have the greatest amount of observational data. These data provide the opportunity to test the theories of stellar interiors and atmospheres.

1.1.1 Solar Magnetic Activity

Magnetic fields are responsible for almost all active phenomena we see on the Sun. Sunspots, prominences and flares are but a few of the most obvious phenomena. Of these, the best-known manifestations of solar magnetic activity are sunspots.

Sunspots

Sunspots are dark parts of the Sun's surface which are significantly cooler than the surrounding area. Sunspots range in size up to ~ 30 x 10^6 m and usually develop and decay over periods of a few days to weeks. Sunspots are significantly cooler (~ 4000 K) than the surrounding photosphere (~ 5780 K).

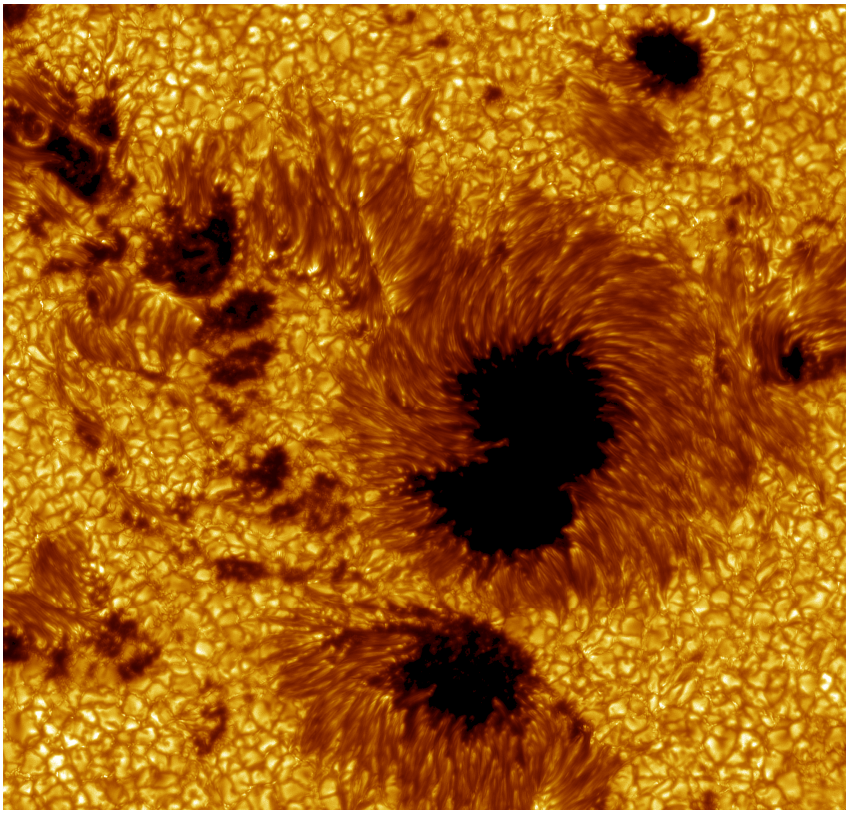

Figure 1.1 A complex sunspot group taken 15 July 2002 by the 1 metre Swedish Solar Telescope on La Palma. This shows the darkening of the sunspot area compared with the surrounding photosphere. (Obtained from web site http://www.solarphysics.kva.se/; Royal Swedish Academy of Sciences)

Sunspots occur where the solar magnetic field breaks through the surface. The presence of the intense magnetic field retards the normal convective process in the photosphere. Sunspots are generally found in groups (see Figure 1.1), and typically a dominant sunspot leads the group in the direction of solar rotation and one or more sunspots follow. Despite the complexity of sunspot groups and the attendant magnetic fields in the region of a sunspot group, the field is essentially bipolar with the trailing spots having the opposite polarity to the leading spot.

The number of sunspots visible on the solar surface varies according to an 11-year cycle (Figure 1.2, lower panel). This was first noted by Heinrich Schwabe in 1843. In

fact, the cycle lasts 22-years: each 11-year cycle is followed by a reversal in the direction of the Sun's magnetic field.

While an individual sunspot remains at a constant latitude, during the solar cycle, the latitudes of new sunspots slowly migrate towards the equator (Figure 1.2, upper panel). However, they usually appear in a band no further than 40° and no closer than 5° either side of the equator. The migration of sunspots results in the famous "butterfly diagram".

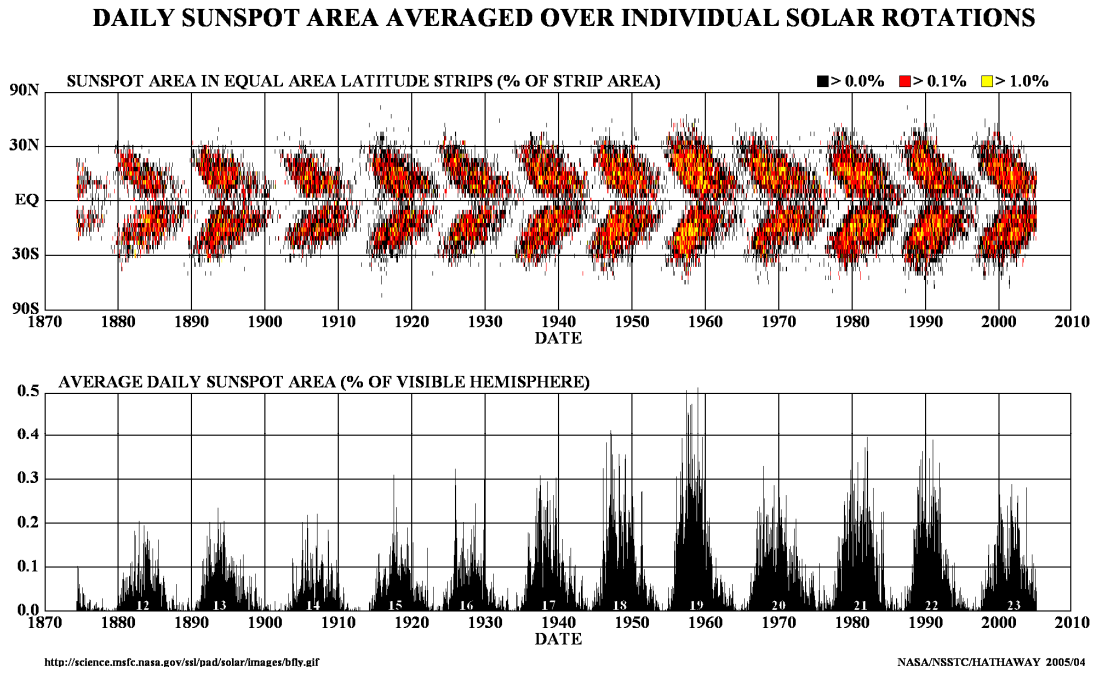

Figure 1.2 Solar butterfly (upper) and sunspot coverage (lower) diagrams from 1874 until 2004. The butterfly diagram (above) shows how the sunspot locations migrate towards the equator during the 11-year solar cycle. The lower diagram shows how the coverage of the solar disc changes over the same cyclical period. Diagram from D.H. Hathaway, NASA Marshall Flight Center. (Obtained from http://science.nasa.gov/ssl/pad/solar/images/bfly.gif)

1.1.2 The Solar Interior

The interior of the Sun consists of 3 layers: the core, the radiative zone and the convective zone (see Figure 1.3).

The core is where thermonuclear reactions take place to convert hydrogen into helium via the proton-proton chain. The core occupies around one quarter of the solar radius, but contains ~ 50% of the solar mass. The boundary between the core and the radiative zone is defined as where the density and temperature fall below that required for nuclear reactions to occur.

In the radiative zone energy from the core is absorbed and re-emitted in random directions. This so-called "random walk" process from the core to the convective zone can take up to one million years. It is believed that the radiative zone rotates almost as a solid body, and recent observations by the SOHO spacecraft confirm this (see Figure 1.4). The radiative zone extends from the core to approximately 75% of the stellar radius.

Finally, the convective zone is the outermost layer of the solar interior. At the base of the convective zone, the temperature is only around 2×10^6 K. At this point, some of the heavier ions such as iron, calcium and nitrogen can retain some of their electrons, which makes the stellar material more opaque to radiation. This traps heat which makes the fluid unstable and it starts to convect. The convective actions carry heat to the stellar surface quite rapidly. The stellar material cools and expands as it rises, resulting in the surface temperature of ~ 5780 K.

The upper layer of the Sun is fluid in nature, and so the equator rotates at a different rate than the poles (differential rotation). This has been known since Galileo first started tracking sunspots. Measurements from the SOHO spacecraft indicate that this rotation is maintained through the convective zone (see Figure 1.4). However, at the point where the radiative zone transitions to the convective zone, the fluid motions of the

convective zone disappear. This change in fluid flow characteristics results in rotationally generated shears. This interface layer plays a key part in the generation of the solar magnetic field.

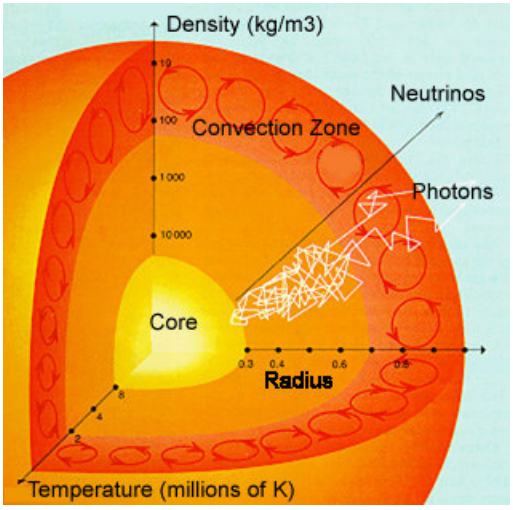

Figure 1.3 The solar interior. The temperature and density of the stellar material falls rapidly as distance from the stellar core increases. (Taken from web site: http://cse.ssl.berkeley.edu/segwayed/lessons/sunspots/research2.html)

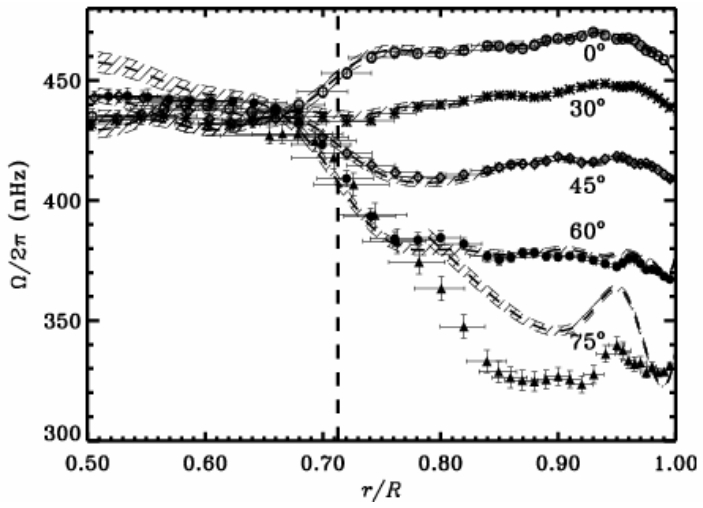

Figure 1.4 Measurements from the SOHO spacecraft show that differential rotation is maintained through the convective zone. Angular velocity is plotted as a function of radius for several selected latitudes. The dashed line indicates the base of the convective zone. Based on data from the Michelson Doppler Imager (MDI) instrument aboard the SOHO spacecraft, averaged over 144 days. Notice that this differential rotation disappears once the radiative zone is reached, confirming the speculation that the radiative zone rotates as a solid body. From Thompson et al. (2003).

1.2 The Solar Dynamo

The solar magnetic field is thought to be generated by the motions of fluid plasma in the interface layer between the radiative and convective zones, known as the tachocline. Kinetic energy is transformed into magnetic energy via a magnetohydrodynamic process and this flux eventually emerges at the solar surface.

1.2.1 The Babcock Model

Babcock (1961) posited that the mechanisms which comprise the Sun's magnetic cycle and therefore the dynamo which is responsible are threefold. The process described below is illustrated in Figure 1.5.

Stage 1: The Ω Effect

Initially, the overall solar magnetic field is approximated by a poloidal dipole field symmetric about the Sun's rotational axis. This original poloidal field is transformed into a toroidal field (where the magnetic field lines are wrapped around the Sun) due to differential rotation. This is called the Ω effect.

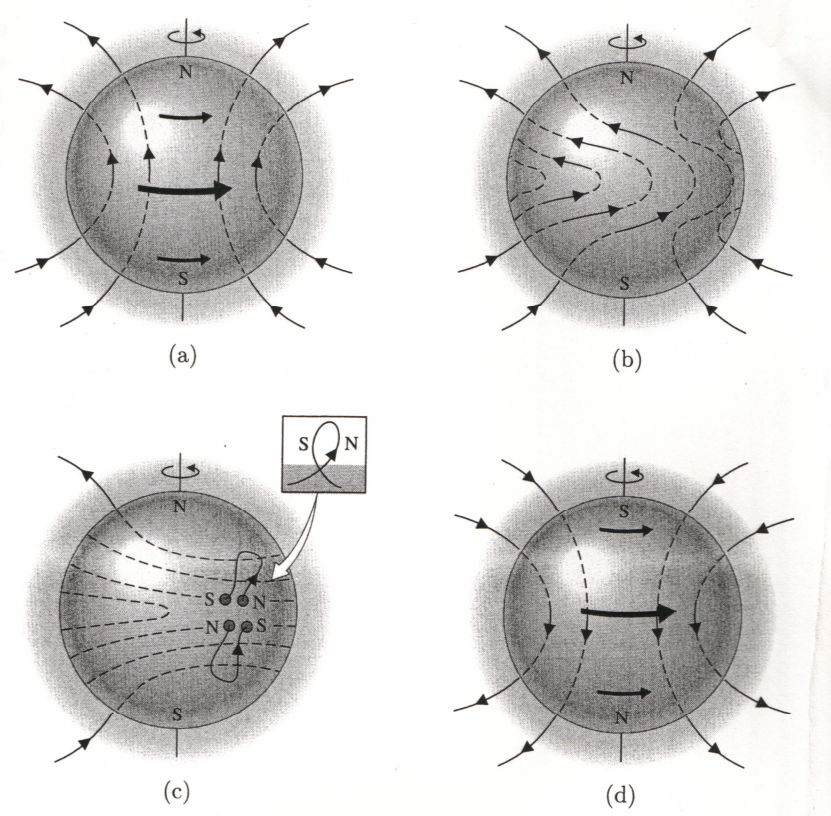

Figure 1.5 The Solar Cycle. The initial poloidal field (a) is twisted into a toroidal field (b) by differential rotation (the Ω effect). Turbulent convection twists the field lines into magnetic ropes (c, the α effect). As the cycle progresses, successive sunspot groups migrate toward the equator where magnetic field reconnection reestablishes the poloidal field, with reversed polarity (d). (Carroll and Ostlie, 1996)

Stage 2: Surface Eruption and the α Effect

Turbulent convection then twists the magnetic field lines into magnetic ropes – regions of intense magnetic fields. This is known as the α effect. The buoyancy produced by magnetic pressure causes the magnetic ropes to rise to the surface. At this point, bipolar active regions are formed as the toroidal flux tubes erupt through the solar surface.

The α effect results in sunspot groups that obey Joy's law – the leading spot of a bipolar pair is located at a lower latitude than the trailing spot. Thus the following spot polarity has a greater chance of migrating to the pole than the leading polarity.

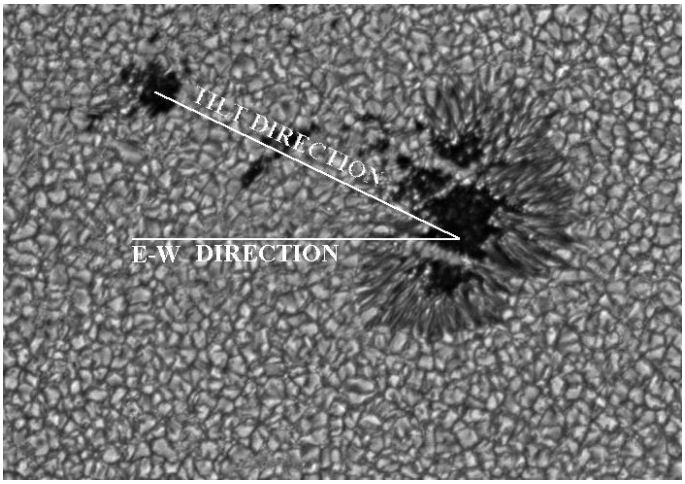

Figure 1.6 Joy's Law. The leading spot of a bipolar pair is located at a lower latitude than the following spot. (From website http://science.msfc.nasa.gov/ssl/pad/solar/images/joys_law.jpg)

In combination, these effects act to neutralize and reverse the global poloidal field.

Stage 3: Opposite Polarity

Finally, the process is repeated with a reversed polarity. Stages 1 and 2 take approximately 11 years. The repetition with the reversed polarity results in the full 22-year solar cycle.

1.2.2 A Refined Model

While the Babcock model illustrates the major parts of the magnetic cycle, it is not complete and is a simplified view. For example, the Babcock model of the Sun's dynamo assumed that the twisting is produced by the effects of the Sun's rotation on very large convective flows that carry heat to the Sun's surface. However, this assumption resulted in amounts of twisting that were far too much and produced magnetic cycles that are only two or three years in length.

Schrijver and Zwaan (2000) present a more refined model than Babcock. Density stratification in the convective zone makes solar convection highly anisotropic. Upflows are weak and broad, while downflows are characterized be a complex, evolving network of lanes and plumes. These downflow plumes are turbulent and they possess substantial rotational components which may amplify fields through the α effect. These fields are then moved downward by the anisotropic convection and accumulate in the overshoot region. Plumes may pull some of this flux upwards and return it to the convection zone where further amplification may take place before being pumped down again. Differential rotation in the tachocline (the Ω effect) creates strong, coherent toroidal flux tubes by stretching and amplifying the disorganized field. As the field becomes stronger, it rises toward the surface in blobs. The Coriolis force acting on these blobs twists them in a systematic way which depends on latitude (the α effect). Weaker structures can be destroyed by turbulent convection, but stronger fields remain coherent and emerge from the surface as bipolar active regions.

Where an active region is close to the pole, the following (i.e. higher latitude) polarities reconnect with the magnetic field at the pole, while leading polarities tend to connect with other active regions. Eventually, the active regions nearest the equator in opposite hemispheres reconnect. These reconnected loops now have a poloidal component which is in the correct direction for the next part of the magnetic cycle. The flux then retracts into the convective zone and the interface layer receives a reversed poloidal field which is then converted into a toroidal field by the Ω effect again.

1.3 Solar-Type Stars

While there is an understanding of the solar dynamo, this understanding is broad and many of the details are unknown. For example, the mechanisms of flux retraction are as yet unknown and unobserved. Studying stars other than the Sun allows the expansion of knowledge about dynamos in general and the refinement of the understanding of the solar dynamo in particular.

The Sun is a main-sequence G2 dwarf, and as has been noted previously, the Sun has a radiative and a convective zone. We can broadly define stars with the same interior structure as the Sun as "solar-type" stars. Stars which have a mass greater than approximately 1.3 solar masses lack a convective zone, while stars of mass lower than approximately 0.3 solar masses should be entirely convective. This encompasses stars from mid-F to early-M spectral types.

1.3.1 Stellar Dynamos

Given that solar-type stars have similar internal structure as the Sun, these stars should exhibit dynamo processes and hence magnetic phenomena in their atmospheres. In fact it has been shown that this is the case (Cram and Kuhi, 1989).

However, while in the solar dynamo it is assumed that the regeneration of the poloidal field is as a result of the α effect, it is theoretically possible for the regeneration to be as a result of the α effect or the Ω effect (i.e. differential rotation). This gives rise to three different dynamo processes:

- $\alpha\Omega$: This is the type of dynamo exhibited by the Sun. In this type of dynamo, periodic behaviour is observed, and the field structures generated are asymmetric. The α term is much smaller than the Ω in the conversion of the poloidal field into a toroidal structure.
- α^2: The type of dynamo exhibited by the Earth. This dynamo generates symmetrical field structures. The Ω component is much smaller than the α, which becomes dominant in the poloidal regeneration and toroidal construction.
- $\alpha^2\Omega$: In this dynamo, the α and Ω terms are of similar magnitude in the generation of the toroidal field.

While present theory indicates that the solar dynamo is generated in the interface layer between the radiative and convective zones, Donati et al. (1992; 1999; 2003a) , Donati and Cameron (1997) and Donati (1999) have indicated that active solar-type stars may exhibit what has been termed a distributed dynamo – where the dynamo process is distributed throughout the convective zone of the star.

While this means that the study of stellar magnetic fields may not be directly applicable to solar study, it is valuable in describing the continuum of dynamo processes, and in fact may be valuable in describing historical aspects of the Sun's magnetic field; especially when the Sun was young and rotating much faster than presently. Magnetism is undeniably a strong influence on the behaviour of the Sun, and so it may be on solar-type stars irrespective of the dynamo mechanism they individually exhibit.

1.4 Stellar Magnetic Activity

Given that solar-type stars have a similar internal structure to the Sun, and given that magnetic phenomena are visible on the Sun, it is reasonable to assume that similar magnetic phenomena should be present on solar-type stars. In fact this is the case, with observations of different types showing the presence of magnetic activity similar to that of the Sun.

1.4.1 Starspots

Starspots, like sunspots are darker areas which are cooler than the surrounding stellar surface due to magnetic activity. As a star rotates, starspots moving across the visible hemisphere of the star result in small variations in brightness (of the order of 0.1 magnitude or less).

Doppler Imaging

Even the nearest dwarf stars to the solar system are so distant that even the largest telescopes cannot resolve their surfaces. Doppler Imaging (also known as DI) is a spectroscopic method which can be used to determine the distribution of starspots across the stellar surface.

Vogt and Penrod (1983) coined the term Doppler Imaging in relation to stellar surface imaging and since this seminal paper, many stars (over 50) have been investigated using the technique.

On a rapidly-rotating star, the individual spectral lines are broadened by the Doppler effect (see Figure 1.7; left panel). The presence of a dark spot results in a

"bump" in the observed spectral line profile (Figure 1.7; right panel). In addition, because the light is "missing" from the dark spot, a slight reduction in the overall intensity of the spectral line is observed. As the star rotates, carrying the dark spot across the stellar disc, the bump in the line profile changes its Doppler shifted position relative to the stellar rotation axis – the bump moves across the line profile.

By observing the star over a series of rotational phases, a map of the locations of starspots on the stellar surface may be created. The principles of Doppler Imaging are described in depth in Vogt et al. (1987), Rice et al.(1989) and Hussain, (1999).

In order to obtain sufficient resolution in longitude, Doppler Imaging is only effective when the stellar target rotates relatively rapidly ($v \sin i \gtrsim 20$ kms^{-1} – cf. solar $v \sin i \approx 2$ kms^{-1}). With very few exceptions (such as EK Dra; Strassmeier and Rice (1998)) most of the stars to date investigated using Doppler Imaging have $v \sin i$ greater than 20 kms^{-1} with some ranging up to ~ 130 kms^{-1} ("Speedy Mic"; Barnes et al. (2000)) and beyond (VXR45A rotates at ~ 248 kms^{-1} (Marsden et al. (2004)).

To date, for solar-type stars, the technique of Doppler Imaging has been exclusively applied to G and K dwarfs (see Strassmeier, 2001). Almost always, these objects observed have exhibited polar spots in addition to many low- and high-latitude features. This is in contrast to the Sun where sunspots exclusively inhabit bands ~ ± 30° either side of the equator.

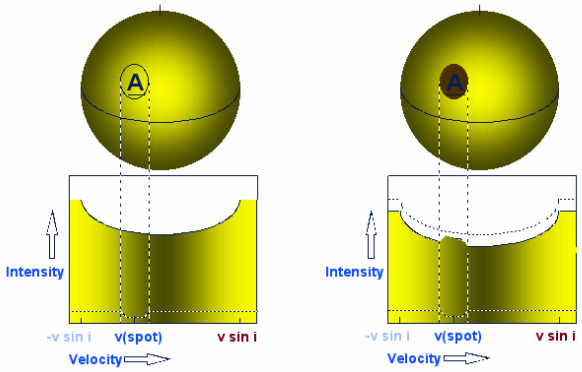

Figure 1.7 The spectral line of a rapidly rotating star is broadened by the Doppler effect (left panel – full stellar disc). The presence of a dark spot (A) in the right panel results in (1) a continuum effect due to the missing light from the spot and (2) a bump in the profile which is Doppler shifted by an amount corresponding to its distance from the stellar rotation axis. (From slides from review talk given at the International Workshop on Astro-tomography, Brussels by Andrew Collier-Cameron (July 2000). Obtained from http://star-www.st-and.ac.uk/~acc4/coolpages/dopreview/sld003.htm).

Schüssler et al. (1996) and Granzer et al. (2000) have done theoretical work on the emergence of flux tubes and the resulting location of star spots. They show that only the very youngest stars which exhibit deep convective zones should have polar spots. Zero-age main sequence objects should show spots which appear at higher latitudes as rotational rates increase, but never exhibit true polar spots. These theoretical studies gave rise to debates about whether polar spots were real or simply artifacts of the techniques used to construct maps. Papers on the subject include Byrne, 1996; Unruh and Cameron, 1997. Flux emergence models such as those in Granzler et al (2000) cannot explain the observation of polar spots on main sequence stars, however polar spots can be explained if magnetic flux tubes undergo a migration towards the pole. It now seems generally accepted that the phenomenon of polar spots is actual rather than artifactual. A new study of the eclipsing binary SV Cam (Jeffers et al., 2005) has also shown direct evidence of a polar spot existing on the primary star of the system.

In addition to polar spots, Donati et al. (2003a) show that for rapidly-rotating solar-type stars, spot coverage can be up to ~ 10% of the visible stellar surface. This is a conservative measurement, given that the mapping techniques minimize the spot area required to fit the observed profiles. In any case, this proportion of spot coverage is over ten times that observed on the solar surface.

The presence of polar spots and the large spot coverage would tend to indicate that either the dynamo processes in these rapidly-rotating solar-type stars are much stronger than those in the Sun, or that the dynamo processes are fundamentally different to the solar dynamo, or both.

1.4.2 Stellar Surface Magnetic Field

In the presence of a magnetic field, spectral lines are seen to split. This is known as the Zeeman effect. While star- and sunspots are manifestations of surface magnetic fields, the Zeeman effect has the potential to allow the direct investigation of the magnetic fields themselves.

When encountering a magnetic field parallel to the line-of-sight, light from the source is split into three components: two symmetric oppositely circularly polarized σ-components and a central linearly-polarized π-component. When the magnetic field is perpendicular to the line-of-sight, the σ-components are linearly polarized perpendicular to the magnetic field and the π-component linearly polarized parallel to the magnetic field. The polarization parameters are often expressed in terms of the Stokes parameters, where parameter I is a measure of the total power in the wave, Q and U represent the linearly polarized components, and V represents the circularly polarized component.

While some work has been done in measuring the magnetic field directly based on the Zeeman effect on certain sensitive lines in stellar spectra (Saar, 1988), the effect is small, and also results in only the average field over the entire visible stellar surface. Hence, these methods do not reveal any information about the magnetic field topology.

Zeeman Doppler Imaging

Zeeman Doppler Imaging (also known as ZDI) is a technique which is used to detect stellar magnetic fields and also resolve the geometry of the magnetic field across the stellar surface. Other methods which integrate the field over the stellar surface cannot do this as features of opposite polarity cancel each other out. Utilizing high resolution echelle spectropolarimeters, stellar magnetic fields can be detected through the Zeeman signatures they generate in the shape and polarization state of spectral line profiles. Initially suggested by Semel (1989), the technique utilizes the same mechanisms as Doppler Imaging (DI) to provide longitudinal resolution, combined with the polarization information which gives information about the orientation of the magnetic field. Donati et al. (2003a) illustrate the ability to map the three components of the magnetic field (azimuthal, meridional and radial).

Like conventional DI, ZDI is best applied to rapidly-rotating stars because the signatures of individual unipolar magnetic regions are associated with different Doppler velocities. This means that bipolar pairs of magnetically active regions no longer mutually cancel each other out as in methods which average the entire surface of the stellar disc.

Semel (1989), Donati et al. (1989), Brown et al. (1991), Donati and Brown (1997), and Donati et al. (2003a) all provide details on the ZDI technique. The basic principles of ZDI are illustrated in Figure 1.8. The visible disc of the star can be divided into regions of equal rotational velocity. As mentioned in Section 1.4.1, spectral lines are broadened by the Doppler effect, and the zones of equal rotational velocity contribute to the spectral lines at a position corresponding to their Doppler wavelength shift. A region of magnetic activity on the visible disc will result in the polarization of the light emerging from that area of the star. By observing in left- and right-hand circularly polarized light, information on the direction and strength of the localized magnetic field can be derived.

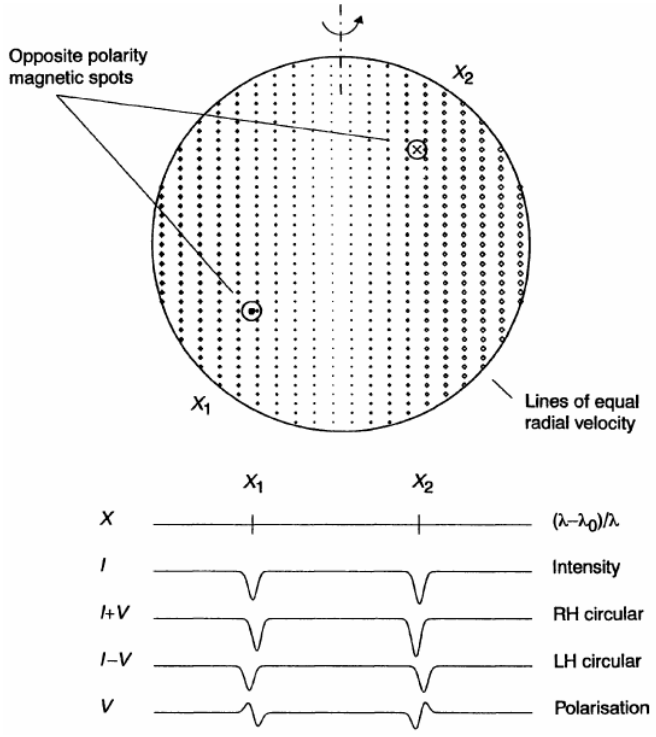

Figure 1.8 Principles of Zeeman Doppler Imaging. Two arbitrary magnetic regions of opposite polarity are present on the stellar disc. The contributions to the stellar spectral line from each of the spots appear at X_1 and X_2, separated by Doppler shift in the wavelength domain. The intensity spectrum is I. Each magnetic field induces small opposite wavelengths shifts of the corresponding absorption profile in the right- and left hand circularly polarized spectra ($I + V$ and $I - V$ respectively, where V is the circular polarization Stoke parameter). The difference between the profiles $I + V$ and $I - V$ results in V, which has a characteristic shape based on the location of the magnetic regions on the surface of the star. Image from Carter et. al., 1996)

Consider, as shown in Figure 1.8, two arbitrary magnetic regions of opposite polarity on the stellar disc. The contributions to the stellar spectral line from each of the spots appear at X_1 and X_2, separated by Doppler shift in the wavelength domain. The intensity spectrum is denoted by $I(\lambda)$. Each magnetic field induces small opposite wavelength shifts of the corresponding absorption profile in the right- and left hand circularly polarized spectra ($I + V$ and $I - V$ respectively, where V is the circular polarization Stokes parameter). The difference between the profiles $I + V$ and $I - V$ results in V, which has a characteristic shape based on the location of the magnetic regions on the surface of the star. If the longitudinal resolution provided by the Doppler effect were not present, then the resulting magnetic signature ($V(\lambda)$) would only be an average for the stellar disc because the opposite-polarity fields would either partly or completely cancel each other out.

The magnetic signatures are quite small (~0.1% of the continuum level), and so there are a number of instrumental considerations to maximize the amount of light captured from the star and to minimize instrumental polarization, and these are discussed in Chapter 2. In addition, a star must be bright to be able to make it a viable ZDI target.

In most of the examples of ZDI mapping thus far, it appears that the azimuthal component of the magnetic field is dominant (Donati et al., 2003a). The azimuthal component of the magnetic field is often evident as rings (Donati et al., 2003a; Donati et al., 1999; Donati, 1999). As mentioned in the discussion of dynamo types, this has led Donati et al. (1992; 1999; 2003a) , Donati and Cameron (1997) and Donati (1999) to

postulate that a distributed dynamo is in operation in these stars rather than an interface-layer dynamo such as that seen in the Sun.

1.4.3 Differential Rotation

It has been long known that the Sun exhibits differential rotation. The Sun rotates every 25 days at the equator and takes progressively longer to rotate at higher latitudes, up to 35 days at the poles. (see Figure 1.4). This means that the equator actually laps the poles approximately every 120 days. Both Doppler Imaging and Zeeman Doppler Imaging present a way to measure differential rotation on stars other than the Sun. By observing either spot features or magnetic features on a stellar surface at different epochs separated by several days, the rates of rotation at different latitudes can be calculated.

There are three spectroscopic methods by which this can be achieved. One method is that described by Petit et al. (2002). This method involves the reconstruction of a single image utilizing a data set covering different epochs, assuming a simplified solar-type differential rotation law (of the form $\Omega(l) = \Omega_{eq} - d\Omega \sin^2 l$) and using this in the reconstruction process. Another method involves cross-correlating images from different epochs, again assuming a solar-type law (Weber et al, 2005). Finally, Cameron et al. (2002) have developed a new method which tracks the rotational periods of individual spots on the stellar surface.

The above methods have been used to measure the differential rotation of several solar type dwarfs (see Table 1.1). All of these stars appear to obey a surface differential rotation law with the equator rotating faster than the poles. In all cases (except R58 in the Marsden et. al. 2005 paper), though, the photospheric shear is significantly stronger than the Sun.

Star	Spectral Type	Lap Time (Sun ~ 120d)	References
AB Dor	K1V	~ 110	Donati and Cameron (1997) Cameron and Donati (2002) Cameron et al. (2002) Donati et. al. (2003b)
LQ Lup	G2V-IV	50 ± 10	Donati et al. (2000)
PZ Tel	K0V-IV	86 ± 14	Barnes et al. (2000)
LQ Hya	K0V	~ 80	Kóvári (2002) Donati et al. (2003b)
R58 (=HD 307938)	G2V	~ 45 (2004) ~ 250 (2005)	Marsden et al. (2004) Marsden et al. (2005)
VXR45A	G9V	~ 90	Marsden et al. (2004)

Table 1.1 Listing of stars which have had differential rotation measurements taken using the methods mentioned.

Interestingly, Donati et al. (2003b) have shown that when the magnetic features are used for cross-correlation instead of the surface spot features, the rates of differential rotation are different. This is attributed to the depth in the stellar atmosphere where the different features are formed and shears within the convective zone. This means that differential rotation of different features may provide a mechanism to probe the interiors of solar-type stars.

Also, Donati et al. (2003b) and Cameron and Donati (2002) have observed changes in the rates of differential rotation in the stars AB Dor and LQ Hya over longer time periods. For example, the lap time for AB Dor was seen to vary from 71±6 days to 136±18 days. Donati et al. (2003b) speculate that temporal variations in the rates of differential rotation are due to feedback effects where magnetic energy is converted into kinetic energy and vice versa.

Models of differential rotation developed by Kitchatinov and Rüdiger (1995) and Rüdiger (1998) show that relative differential rotation $\frac{d\Omega}{\Omega_{eq}}$ (where $d\Omega$ is the difference in rotation rate between the pole and equator and Ω_{eq} is the rotation rate at the equator) should decrease in rapid rotators, and should also decrease in stars with larger convective zones. Barnes et al. (2005) demonstrate that differential rotation appears to increase with the stellar temperature. However, the number of observations is still small, and a relationship between differential rotation and various physical stellar parameters is not clear.

1.5 The Active Young F Dwarf HR 1817 (= HD 35850)

HR 1817 (HD 35850) is a remarkably active young F dwarf star. As an F7V dwarf, it is at the warm end of the continuum of solar-type stars and its physical parameters (Table 1.2) such as its rotation rate, level of activity and brightness (Figure 1.9) mean that it is an ideal target for the techniques of Doppler and Zeeman Doppler Imaging.

1.5.1 Physical Parameters of HR 1817

HR 1817 is of spectral type F7V, is a rapid rotator and has intense X-ray and extreme ultraviolet (EUV) emission (Tagliaferri et al., 1997). It also exhibits a strong lithium abundance, indicating its relative youth. For physical parameters, see Table 1.2.

Parameter	Value
Coordinates (2000)	05 27 04.76 -11 54 03.5
Spectral Type	F7V
$v \sin i$	50 km s^{-1}
Distance	26.8 pc
B Magnitude	6.8
V Magnitude	6.3
Age	~ 12 Myr
Radius	1.18 $R_{\odot}$
Mass	1.15 $M_{\odot}$

Table 1.2 Parameters of HR 1817. From Tagliaferri et al. (1997); Gagné et al. (1999); Mathioudakis and Mullan (1999); Zuckerman et al. (2001). Note that none of the original sources quote errors for these values.

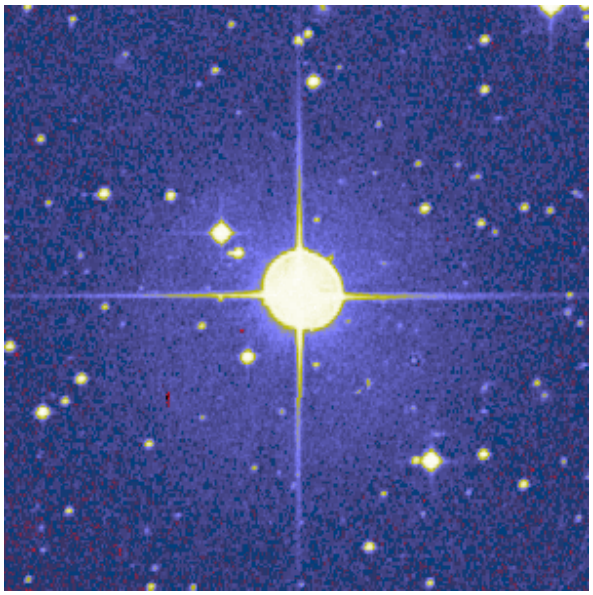

Figure 1.9 HR 1817. Image from NASA SkyView

As Gagné et al. (1999) show, HR 1817 is slightly more massive and larger than the Sun. The star has also been identified as part of the young and nearby β Pictoris moving group (Zuckerman et al., 2001). EUV observations suggest that HR 1817 is in a state of near continuous low-amplitude flaring (Gagné et al., 1999).

The fact that HR 1817 is active and bright made it an attractive target for investigations using Doppler Imaging and Zeeman Doppler Imaging. In addition, photometry of HR 1817 (Budding et al. 2002) indicated slow drifts of ~ 0.04 mag in V over timescales of ~ 3-4 hours. This variation in magnitude is indicative of spots on the star.

On the downside, a photometric period of the star had not been accurately determined. Mathioudakis and Mullan (1999), however determined that the period of HR 1817 was almost exactly one day, based on the only non-systemic periodicity observed during monitoring of the star with the EUVE satellite. A 1-day period is problematic in Doppler and Zeeman Doppler Imaging, as it is very difficult to obtain full phase coverage of the star. However, the technique is robust enough to recover information on the phase coverage that is available. Potentially, in the future, multi-site observations will allow complete phase coverage of HR 1817.

1.6 Summary

It is clear that magnetic activity is an important mechanism in the Sun. The manifestations of magnetic activity on the stellar surface are indicators of what is happening deep within the Sun. Similarly, it is apparent that magnetic phenomena are present in solar-type stars of spectral type G and K.

This dissertation is investigating the magnetic activity on the F dwarf HR 1817. The investigation of active areas and the magnetic topology of HR 1817 will extend the continuum of stellar type investigated using the Doppler Imaging and Zeeman Doppler Imaging techniques. It is hoped that this may give an indication of how the dynamo

processes of a warmer star with a thinner convective zone behave, and whether this assists in the analysis of models of stellar dynamos in solar-type stars.

Chapter 2

Instrumental Setup, Observations and Analysis

2.1 ZDI at the Anglo-Australian Telescope

The Anglo-Australian Telescope is one of the few telescopes in the world used for Zeeman Doppler Imaging. Its 3.9 m mirror, coupled with the University College London Echelle Spectrograph (UCLES) is used with the visitor instrument, the Semel Polarimeter. The polarimeter is placed at the Cassegrain focus of the telescope and light is guided to UCLES via a pair of optic fibres.

Instrumental Considerations

Because the magnetic signatures Zeeman Doppler Imaging searches for are so small, there are stringent requirements for the instrumental setup of which there are three concerns (as outlined in Semel et al., 1993).

- Signal-to-noise Ratio. To reduce the photon noise, the instrumental setup must collect as much light as possible. However, the stars being observed are rapid

rotators, and making the observations too long will smear the Doppler image and reduce the longitudinal resolution. Semel et al. (1993) recommend that the individual exposures are not longer than $1 - 2\%$ of the stellar rotation period. Hence, in addition to ideal targets being bright, a large telescope is essential. HR 1817 is a bright target, and the Anglo-Australian Telescope provides an aperture sufficient to provide the appropriate light-gathering power.

- Spectral Resolution. The smallest scale of stellar feature depends upon the ratio of rotational line broadening to instrumental broadening. At the AAT, Semel et al. (1993) and Donati et al. (2003a) are able to achieve spectral resolution of 70,000 using UCLES.
- Reduction of Instrumental/Spurious Polarization Signals. These should be reduced to the level of photon noise or less. Mounting the polarimeter at the Cassegrain focus of the AAT and the fibre-optic feed used with the Semel polarimeter eliminates the coudé mirror train at the AAT, eliminating oblique mirror polarization effects. The design and operation of the Semel polarimeter also reduces other instrumental polarization effects.

Semel Polarimeter

The Semel polarimeter is conceptually arranged as in Figure 2.1. A quarter-wave plate is used to obtain the circularly polarized light. Optimally, the quarter-wave plate should have a linear retardance of 90° and its axes rotated 45° to the axis of the beam splitter.

To eliminate crosstalk from the linear to circular polarization, two exposures are used, between which the quarter-wave plate is rotated 90°. The opposite polarizations are interleaved on the CCD and swapped between exposures to minimize instrumental

polarization. Since the observing of 2001/2002, a new Semel polarimeter was used. Instead of physically rotating the quarter-wave plate (which generated physical beam displacement) a half-wave plate was included after the quarter-wave plate, which was rotated instead. This eliminated the need for beam displacement (Donati et al., 2003a).

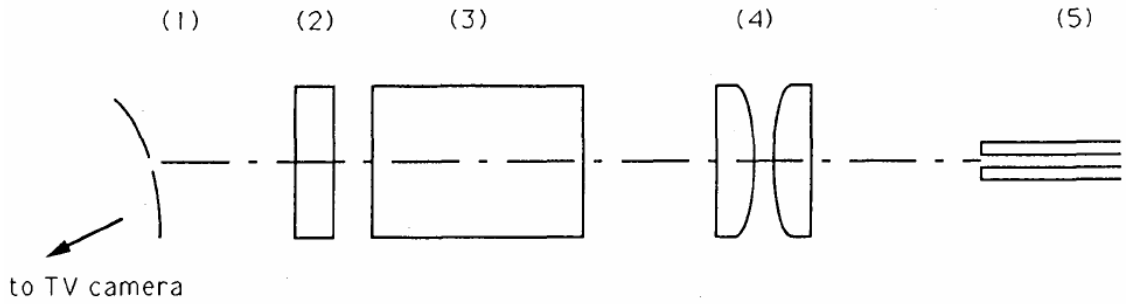

Figure 2.1 Polarimeter Package as used at the Canada-France-Hawaii Telescope (CFHT), but the concept at the AAT is the same. 1. Spherical mirror with an aperture where the star image is formed. 2. Quarter wave plate which may be rotated to ±45° to the polarization axes of the beam splitter. 3. An aberration-free beam splitter. 4. Focal reducer. The first doublet has a hole at its focal plane; the second forms two images of the star. 5. The two optical fibres at the entrance of which the images are formed. The fibres transmit the light to a spectrograph. From Semel et al., 1993).

Operationally, for Zeeman Doppler Imaging we take sequences of four images in the alternating polarization positions of the Semel polarimeter. Four separate exposures allow the use of a null measurement technique, as described in more detail in Section 2.3 of this thesis. The sequences are done P1-P2-P2-P1 where P1 is in one polarization position, P2 in polarization position 2, orthogonal to P1.

2.1.1 Instrumental Setup

Initial Detection: 9 December 2000

The ZDI instrumental setup used to collect the data for the initial attempt at the detection of the magnetic field of HR 1817 is similar to that described in Donati et al. (1997; 1999); Donati and Cameron (1997); Donati (1999), but especially Donati et al. (2003a).

The Semel polarimeter was mounted at the Cassegrain focus of the 3.9 m Anglo-Australian Telescope (AAT). A dual optical fibre (one for each of the oppositely circularly polarized beams) then guides the light to UCLES via a Bowen-Walraven image slicer, set to a two slice per fibre configuration. The Cassegrain mounting and the fibre-optic transport mechanism are utilized to minimize instrumental polarization effects due to mirror reflections. At the AAT, these methods eliminate the normal coudé optical train usually used with UCLES.

In 2000, the Donati team used the MIT/LL2A CCD detector (see http://www.aao.gov.au/local/www/cgt/ccdimguide/mitll2a.html for detector specifications). The MIT/LL2A detector consists of 2048 (horizontal) x 4096 (vertical) 15 μm pixels. The detector is larger than the unvignetted field of UCLES, and as such a window of 2048 x 2448 pixels was used to reduce read-out time. Using the 31.6 groove mm^{-1} grating, 52 orders (numbers 80 to131) can be fully recorded, covering 430 nm to 715 nm. With the slit projecting onto 29 x 2.5 pixels, a spectral resolution of approximately 70,000 with a pixel size of approximately 1.9 km s^{-1} is obtained.

Doppler and Zeeman Doppler Imaging: 23 December 2001 – 2 January 2002

Again, the ZDI instrumental setup used to collect the data for the imaging of HR 1817 (over the period 23 December, 2001 until January 2, 2002) is similar to that described in Donati et al. (2003a) and elsewhere (Donati et al. (1997; 1999); Donati and Cameron (1997); Donati (1999)).

As described above, the Semel polarimeter was mounted at the Cassegrain focus of the 3.9 m Anglo-Australian Telescope (AAT). A dual optical fibre (one for each of the oppositely circularly polarized beams) then guides the light to UCLES via a Bowen-Walraven image slicer, set to a two slice per fibre configuration.

In observing sessions prior to 2001/2002, the Donati team used the MIT/LL2A CCD detector. During December 2001 to January 2002, the AAT's new EEV detector. (see http://www.aao.gov.au/local/www/cgt/ccdimguide/eev.html for detector specifications) was used. The EEV detector consists of 2048 (horizontal) x 4096 (vertical) 13.5 μm pixels. Like the MIT/LL2A, the EEV detector is larger than the unvingetted field of UCLES, and as such a window of 2048 x 2746 pixels was used to reduce read-out time. Also, the reduced window meant that vignetting within the UCLES camera should only be around 10% larger on the order edges than at the centre. Using the 31.6 groove mm^{-1} grating, 46 orders (numbers 84 to129) can be fully recorded, covering 437 nm to 681 nm.

With the slit projecting onto 33 x 2.7 pixels, a spectral resolution of approximately 70,000 with a pixel size of approximately 1.7 km s^{-1} is obtained.

2.2 Observations

Initial Detection: 9 December 2000

On December 9, 2000, 16 observations of HR 1817 were taken over a period of approximately 2 hours. The purpose of this run was to attempt a detection of the magnetic field of HR 1817. All exposures were 300 seconds long and all images were of good quality with high signal-to-noise and were used in the detection process. The list of observations is shown in Table 2.1.

Table 2.1 Log of observations of HR 1817, 9 December 2000. The exposure numbers are those from the night and are not necessarily sequential as other targets were also being observed. The polarization position refers to the two orthogonal positions of the quarter-wave plate P1 and P2.

Date	Exposure Number	UT Date	UT Start	UT End	Polari-zation Position	Exposure Time (s)
December 9, 2000	21	2000:12:09	09:55:36.68	10:00:36	P1	300
	22	2000:12:09	10:01:53.56	10:06:53	P2	300
	23	2000:12:09	10:08:04.67	10:13:04	P2	300
	24	2000:12:09	10:14:16.04	10:19:16	P1	300
	25	2000:12:09	10:20:23.93	10:25:24	P1	300
	26	2000:12:09	10:26:35.92	10:31:36	P2	300
	27	2000:12:09	10:32:45.83	10:37:46	P2	300
	28	2000:12:09	10:38:57.18	10:43:58	P1	300
	33	2000:12:09	11:10:30.25	11:15:30	P1	300
	34	2000:12:09	11:16:41.36	11:21:42	P2	300
	35	2000:12:09	11:22:49.91	11:27:49	P2	300
	36	2000:12:09	11:29:03.67	11:34:03	P1	300
	37	2000:12:09	11:35:11.58	11:40:11	P1	300
	38	2000:12:09	11:41:28.93	11:46:28	P2	300
	39	2000:12:09	11:47:38.76	11:52:38	P2	300
	40	2000:12:09	11:53:48.43	11:58:48	P1	300

Doppler and Zeeman Doppler Imaging: 23 December 2001 – 2 January 2002

From December 23, 2001 until January 2 2002, a total of 204 observations of HR 1817 were taken over the four nights of 23 December, 26 December, 30 December and 2 January. With one exception (where the exposure time was extended to 300 seconds, due to poor weather), all exposures were 200 seconds long. The list of observations is shown in Table 2.2. While cloud interrupted some nights, and caused some of the 4-exposure sequences to be aborted, all frames taken were usable for Doppler Imaging, and most of the sequences were useable for Zeeman Doppler Imaging.

Table 2.2 Log of observations of HR 1817, 23 December 2001 – 2 January 2002. The exposure numbers are those from the particular night and are not necessarily sequential as other targets were also being observed. The phase is based on a rotational period of 1 day, and zero phase was taken to be approximately half-way though the run. The observations thus spanned over 10 complete rotations of HR 1817. The polarization position refers to the two orthogonal positions of the quarter-wave plate P1 and P2.

Date	Exposure Number	UT Date	UT Start	UT End	Polari-zation Position	Exposure Time (s)	Phase
December 23, 2001	24	2001:12:23	09:54:16.97	09:57:37	P1	200	-5.0862
	25	2001:12:23	09:59:00.80	10:02:21	P2	200	-5.0829
	26	2001:12:23	10:03:36.31	10:06:57	P2	200	-5.0797
	27	2001:12:23	10:08:12.70	10:11:34	P1	200	-5.0765
	28	2001:12:23	10:12:49.48	10:16:09	P1	200	-5.0733
	29	2001:12:23	10:17:24.82	10:20:45	P2	200	-5.0701
	30	2001:12:23	10:22:00.81	10:25:22	P2	200	-5.0669
	31	2001:12:23	10:26:37.27	10:29:57	P1	200	-5.0637
	32	2001:12:23	10:31:12.63	10:34:33	P1	200	-5.0606
	33	2001:12:23	10:35:58.04	10:39:19	P2	200	-5.0573
	34	2001:12:23	10:40:36.03	10:43:56	P2	200	-5.054
	35	2001:12:23	10:45:11.77	10:48:32	P1	200	-5.0508
	36	2001:12:23	10:49:46.96	10:53:07	P1	200	-5.0477
	37	2001:12:23	10:54:22.22	10:57:42	P2	200	-5.0445
	38	2001:12:23	10:58:58.04	11:02:18	P2	200	-5.0413
	47	2001:12:23	16:24:43.52	16:28:03	P1	200	-4.8151
	48	2001:12:23	16:29:18.63	16:32:39	P2	200	-4.8119
	49	2001:12:23	16:33:55.17	16:37:15	P2	200	-4.8087
	50	2001:12:23	16:38:31.00	16:41:51	P1	200	-4.8055
	51	2001:12:23	16:43:27.30	16:46:47	P1	200	-4.8021
	52	2001:12:23	16:48:02.73	16:51:23	P2	200	-4.7989
	53	2001:12:23	16:52:38.47	16:55:58	P2	200	-4.7957
	54	2001:12:23	16:57:14.14	17:00:34	P1	200	-4.7925
	55	2001:12:23	17:01:49.64	17:05:10	P1	200	-4.7893
	56	2001:12:23	17:06:24.99	17:09:45	P2	200	-4.7861
	57	2001:12:23	17:11:02.02	17:14:22	P2	200	-4.7829
	58	2001:12:23	17:15:37.21	17:18:57	P1	200	-4.7797
	59	2001:12:23	17:20:17.27	17:23:37	P1	200	-4.7765
	60	2001:12:23	17:24:53.26	17:28:13	P2	200	-4.7733
	61	2001:12:23	17:29:30.03	17:32:50	P2	200	-4.7701
	62	2001:12:23	17:34:05.62	17:37:26	P1	200	-4.7669
December 26, 2001	29	2001:12:26	10:01:33.64	10:04:54	P1	200	-2.0811
	30	2001:12:26	10:06:08.91	10:09:29	P2	200	-2.078
	31	2001:12:26	10:10:44.49	10:14:04	P2	200	-2.0748
	32	2001:12:26	10:15:20.25	10:18:40	P1	200	-2.0716
	33	2001:12:26	10:20:11.51	10:23:32	P1	200	-2.0682
	34	2001:12:26	10:24:48.21	10:28:08	P2	200	-2.065
	35	2001:12:26	10:29:23.87	10:32:44	P2	200	-2.0618
	36	2001:12:26	10:33:58.98	10:37:19	P1	200	-2.0586

Date	Exposure Number	UT Date	UT Start	UT End	Polari-zation Position	Exposure Time (s)	Phase
	37	2001:12:26	10:38:36.57	10:41:57	P1	200	-2.0554
	38	2001:12:26	10:43:12.47	10:46:32	P2	200	-2.0522
	39	2001:12:26	10:47:47.97	10:51:09	P2	200	-2.049
	40	2001:12:26	10:52:33.31	10:55:53	P1	200	-2.0457
	41	2001:12:26	10:57:09.06	11:00:30	P1	200	-2.0425
	42	2001:12:26	11:01:45.37	11:05:07	P2	200	-2.0393
	43	2001:12:26	11:06:22.15	11:09:43	P2	200	-2.0361
	44	2001:12:26	11:11:04.61	11:14:25	P1	200	-2.0329
	45	2001:12:26	11:15:41.00	11:19:01	P1	200	-2.0297
	46	2001:12:26	11:20:16.43	11:23:37	P2	200	-2.0265
	47	2001:12:26	11:24:52.25	11:28:12	P2	200	-2.0233
	48	2001:12:26	11:29:29.52	11:32:50	P1	200	-2.0201
	49	2001:12:26	11:34:05.26	11:37:25	P1	200	-2.0169
	50	2001:12:26	11:38:41.25	11:42:01	P2	200	-2.0137
	51	2001:12:26	11:43:16.76	11:46:37	P2	200	-2.0105
	52	2001:12:26	11:47:52.42	11:51:12	P1	200	-2.0073
	57	2001:12:26	12:18:06.72	12:21:27	P1	200	-1.9863
	58	2001:12:26	12:22:42.23	12:26:02	P2	200	-1.9831
	59	2001:12:26	12:27:17.89	12:30:38	P2	200	-1.9799
	60	2001:12:26	12:31:53.71	12:35:14	P1	200	-1.9767
	61	2001:12:26	12:36:29.14	12:39:49	P1	200	-1.9736
	62	2001:12:26	12:41:04.88	12:44:26	P2	200	-1.9704
	63	2001:12:26	12:45:52.71	12:49:13	P2	200	-1.967
	64	2001:12:26	12:50:28.29	12:53:48	P1	200	-1.9638
	65	2001:12:26	12:55:03.73	12:58:24	P1	200	-1.9607
	66	2001:12:26	12:59:39.63	13:03:00	P2	200	-1.9575
	67	2001:12:26	13:04:15.21	13:07:35	P2	200	-1.9543
	68	2001:12:26	13:08:51.04	13:12:11	P1	200	-1.9511
	69	2001:12:26	13:13:26.32	13:16:46	P1	200	-1.9479
	70	2001:12:26	13:18:01.59	13:21:22	P2	200	-1.9447
	71	2001:12:26	13:22:37.34	13:25:58	P2	200	-1.9415
	72	2001:12:26	13:27:17.48	13:30:37	P1	200	-1.9383
	73	2001:12:26	13:31:53.15	13:35:13	P1	200	-1.9351
	74	2001:12:26	13:36:28.66	13:39:49	P2	200	-1.9319
	75	2001:12:26	13:41:05.12	13:44:25	P2	200	-1.9287
	76	2001:12:26	13:45:40.95	13:49:01	P1	200	-1.9255
	81	2001:12:26	14:30:56.93	14:34:17	P1	200	-1.8941
	82	2001:12:26	14:35:32.83	14:38:54	P2	200	-1.8909
	83	2001:12:26	14:40:09.86	14:43:30	P2	200	-1.8877
	84	2001:12:26	14:44:45.69	14:48:06	P1	200	-1.8845
	85	2001:12:26	14:49:21.83	14:52:42	P1	200	-1.8813
	86	2001:12:26	14:53:57.41	14:57:17	P2	200	-1.8781
	87	2001:12:26	14:58:32.91	15:01:53	P2	200	-1.8749
	88	2001:12:26	15:03:08.82	15:06:29	P1	200	-1.8717
	89	2001:12:26	15:07:44.72	15:11:06	P1	200	-1.8685
	90	2001:12:26	15:12:21.91	15:15:42	P2	200	-1.8653
	91	2001:12:26	15:16:57.98	15:20:18	P2	200	-1.8621

Date	Exposure Number	UT Date	UT Start	UT End	Polari-zation Position	Exposure Time (s)	Phase
	92	2001:12:26	15:21:39.90	15:25:01	P1	200	-1.8589
	93	2001:12:26	15:39:14.36	15:42:35	P1	200	-1.8466
	94	2001:12:26	15:43:50.99	15:47:11	P2	200	-1.8434
	95	2001:12:26	15:48:26.97	15:51:47	P2	200	-1.8403
	96	2001:12:26	15:53:02.80	15:56:23	P1	200	-1.8371
	101	2001:12:26	16:21:18.86	16:24:39	P1	200	-1.8174
	102	2001:12:26	16:25:54.43	16:29:14	P2	200	-1.8142
	103	2001:12:26	16:30:30.09	16:33:50	P2	200	-1.811
	104	2001:12:26	16:35:06.48	16:38:26	P1	200	-1.8078
	105	2001:12:26	16:39:42.29	16:43:02	P1	200	-1.8047
	106	2001:12:26	16:44:17.96	16:47:38	P2	200	-1.8015
	107	2001:12:26	16:48:53.78	16:52:14	P2	200	-1.7983
	108	2001:12:26	16:53:29.85	16:56:50	P1	200	-1.7951
	109	2001:12:26	16:58:05.76	17:01:26	P1	200	-1.7919
	110	2001:12:26	17:03:01.83	17:06:22	P2	200	-1.7885
	111	2001:12:26	17:07:38.14	17:10:58	P2	200	-1.7853
	112	2001:12:26	17:12:13.72	17:15:34	P1	200	-1.7821
	113	2001:12:26	17:16:50.02	17:20:10	P1	200	-1.7789
	114	2001:12:26	17:21:26.01	17:24:46	P2	200	-1.7757
	115	2001:12:26	17:26:01.67	17:29:22	P2	200	-1.7725
	116	2001:12:26	17:30:46.06	17:34:06	P1	200	-1.7692
December 30, 2001	33	2001:12:30	10:32:09.98	10:35:30	P1	200	1.9401
	34	2001:12:30	10:36:46.21	10:40:06	P2	200	1.9433
	35	2001:12:30	10:41:21.24	10:44:41	P2	200	1.9465
	36	2001:12:30	10:45:58.26	10:49:19	P1	200	1.9497
	37	2001:12:30	10:50:37.12	10:53:57	P1	200	1.9529
	38	2001:12:30	10:55:12.79	10:58:33	P2	200	1.9561
	39	2001:12:30	10:59:50.85	11:03:11	P2	200	1.9593
	40	2001:12:30	11:04:26.83	11:07:48	P1	200	1.9625
	41	2001:12:30	11:09:06.50	11:12:28	P1	200	1.9658
	42	2001:12:30	11:13:43.53	11:17:09	P2	200	1.969
	43	2001:12:30	11:18:24.71	11:21:45	P2	200	1.9722
	44	2001:12:30	11:23:01.65	11:26:22	P1	200	1.9754
	45	2001:12:30	11:27:36.60	11:30:57	P1	200	1.9786
	46	2001:12:30	11:32:12.58	11:35:32	P2	200	1.9818
	47	2001:12:30	11:36:48.08	11:40:08	P2	200	1.985
	48	2001:12:30	11:41:23.43	11:44:45	P1	200	1.9882
	53	2001:12:30	12:06:23.58	12:09:44	P1	200	2.0055
	54	2001:12:30	12:10:59.01	12:14:19	P2	200	2.0087
	55	2001:12:30	12:15:34.58	12:18:54	P2	200	2.0119
	56	2001:12:30	12:20:10.02	12:23:31	P1	200	2.0151
	57	2001:12:30	12:24:45.92	12:28:08	P1	200	2.0183
	58	2001:12:30	12:29:23.52	12:32:45	P2	200	2.0215
	59	2001:12:30	12:34:00.23	12:37:21	P2	200	2.0247
	60	2001:12:30	12:38:35.97	12:41:57	P1	200	2.0279
	61	2001:12:30	12:43:14.83	12:46:35	P1	200	2.0311
	62	2001:12:30	12:47:50.18	12:51:10	P2	200	2.0343

Date	Exposure Number	UT Date	UT Start	UT End	Polari-zation Position	Exposure Time (s)	Phase
	63	2001:12:30	12:52:26.00	12:55:46	P2	200	2.0375
	64	2001:12:30	12:57:01.27	13:00:21	P1	200	2.0407
	65	2001:12:30	13:01:36.29	13:04:56	P1	200	2.0439
	66	2001:12:30	13:06:11.65	13:09:32	P2	200	2.0471
	67	2001:12:30	13:10:46.76	13:14:07	P2	200	2.0503
	68	2001:12:30	13:15:28.58	13:18:49	P1	200	2.0535
	69	2001:12:30	13:28:40.44	13:32:01	P1	200	2.0627
	70	2001:12:30	13:33:16.91	13:36:37	P2	200	2.0659
	71	2001:12:30	13:37:52.09	13:41:12	P2	200	2.0691
	72	2001:12:30	13:42:27.77	13:45:49	P1	200	2.0723
	73	2001:12:30	13:47:04.55	13:50:25	P1	200	2.0755
	74	2001:12:30	13:51:41.42	13:55:03	P2	200	2.0787
	75	2001:12:30	13:56:18.28	13:59:38	P2	200	2.0819
	76	2001:12:30	14:00:54.27	14:04:14	P1	200	2.0851
	81	2001:12:30	14:26:21.06	14:29:41	P1	200	2.1027
	82	2001:12:30	14:30:56.41	14:34:17	P2	200	2.1059
	83	2001:12:30	14:35:33.11	14:38:53	P2	200	2.1091
	84	2001:12:30	14:40:08.46	14:43:28	P1	200	2.1123
	85	2001:12:30	15:00:35.25	15:03:55	P1	200	2.1265
	86	2001:12:30	15:24:09.07	15:27:29	P2	200	2.1429
	87	2001:12:30	15:28:44.58	15:32:05	P2	200	2.1461
	88	2001:12:30	15:33:21.05	15:36:41	P1	200	2.1493
	89	2001:12:30	15:37:56.56	15:41:17	P1	200	2.1525
	90	2001:12:30	15:42:33.26	15:45:53	P2	200	2.1557
	91	2001:12:30	15:47:09.88	15:50:30	P2	200	2.1589
	92	2001:12:30	15:51:48.51	15:55:10	P1	200	2.1621
	93	2001:12:30	15:56:29.13	15:59:49	P2	200	2.1653
	98	2001:12:30	16:26:25.43	16:29:46	P1	200	2.1861
	99	2001:12:30	16:31:02.86	16:34:23	P2	200	2.1893
	100	2001:12:30	16:35:38.37	16:38:58	P2	200	2.1925
	101	2001:12:30	16:40:13.39	16:43:33	P1	200	2.1957
	102	2001:12:30	16:44:49.70	16:48:10	P1	200	2.1989
	103	2001:12:30	16:49:30.65	16:52:51	P2	200	2.2022
	104	2001:12:30	16:54:06.80	16:57:27	P2	200	2.2053
	105	2001:12:30	16:58:43.98	17:03:44	P1	300	2.2086
	106	2001:12:30	17:04:59.40	17:08:19	P1	200	2.2129
	107	2001:12:30	17:09:35.09	17:12:55	P2	200	2.2161
	108	2001:12:30	17:14:11.93	17:17:32	P2	200	2.2193
	109	2001:12:30	17:18:47.68	17:22:08	P1	200	2.2225
January 2, 2002					P1		
	24	2002:01:02	10:24:46.46	10:28:07		200	4.935
	25	2002:01:02	10:29:22.70	10:32:43	P2	200	4.9382
	26	2002:01:02	10:33:58.43	10:37:19	P2	200	4.9414
	27	2002:01:02	10:38:34.33	10:41:54	P1	200	4.9446
	28	2002:01:02	10:43:11.04	10:46:31	P1	200	4.9478
	29	2002:01:02	10:47:51.34	10:51:13	P2	200	4.951
	30	2002:01:02	10:52:30.78	10:55:51	P2	200	4.9542
	31	2002:01:02	10:57:07.02	11:00:27	P1	200	4.9574

Date	Exposure Number	UT Date	UT Start	UT End	Polari-zation Position	Exposure Time (s)	Phase
	32	2002:01:02	11:01:45.79	11:05:06	P1	200	4.9607
	33	2002:01:02	11:06:21.31	11:09:41	P2	200	4.9639
	34	2002:01:02	11:10:56.82	11:14:17	P2	200	4.967
	35	2002:01:02	11:15:33.70	11:18:54	P1	200	4.9702
	36	2002:01:02	11:20:10.79	11:23:31	P1	200	4.9735
	37	2002:01:02	11:24:46.38	11:28:08	P2	200	4.9766
	38	2002:01:02	11:29:23.16	11:32:43	P2	200	4.9798
	39	2002:01:02	11:33:58.27	11:37:21	P1	200	4.983
	44	2002:01:02	11:59:26.43	12:02:46	P1	200	5.0007
	45	2002:01:02	12:04:03.85	12:07:24	P2	200	5.0039
	46	2002:01:02	12:08:39.92	12:12:00	P2	200	5.0071
	47	2002:01:02	12:13:16.15	12:16:36	P1	200	5.0103
	48	2002:01:02	12:17:57.82	12:21:18	P1	200	5.0136
	49	2002:01:02	12:22:35.17	12:25:55	P2	200	5.0168
	50	2002:01:02	12:27:15.63	12:30:36	P2	200	5.02
	51	2002:01:02	12:31:52.11	12:35:12	P1	200	5.0232
	52	2002:01:02	12:36:28.82	12:39:49	P1	200	5.0264
	53	2002:01:02	12:41:06.27	12:44:26	P2	200	5.0296
	54	2002:01:02	12:45:42.79	12:49:03	P2	200	5.0328
	55	2002:01:02	12:50:19.02	12:53:39	P1	200	5.036
	56	2002:01:02	12:54:56.45	12:58:17	P1	200	5.0393
	57	2002:01:02	12:59:33.95	13:02:54	P2	200	5.0425
	58	2002:01:02	13:04:09.61	13:07:30	P2	200	5.0457
	59	2002:01:02	13:08:46.15	13:12:06	P1	200	5.0489

2.3 Analysis: Spectral Extraction

The raw frames taken using the instrumental setup described in Section 2.1 need to be converted into wavelength calibrated spectra. To achieve this, a custom-written package called ESpRIT (*E*chelle *Sp*ectra *R*eduction: an *I*nteractive *T*ool) was used. A summary of the operation of ESpRIT is shown here; a much more detailed description can be found in Donati et al. (1997). The code base I used is maintained by Jean-François Donati, and he has kindly provided it for use in my data reduction.

Why use ESpRIT?

Due to the peculiarities of the instrumental setup used for Zeeman Doppler Imaging, Donati et al. decided to develop a dedicated package for image extraction. Each order produced by UCLES include two spectra; one for each polarization state. Also, the use of the Bowen-Walraven image slicer produces a complicated order section profile. The slicer also generates distortion in the slit shape. As discussed in Donati et al. (1997) these peculiarities present difficulties for more conventional data reduction routines.

Because Zeeman Doppler Imaging is searching for very small distortions in spectral lines, spectral resolution must be as high as possible and the data reduction process must result in minimal degradation of the quality of the resultant spectra. Also, the slit tilt and distortion must be taken into account, otherwise it is possible to introduce spurious polarization signals.

The extraction of the calibrated spectra from raw frames takes 3 steps. Firstly, the geometrical features of the raw frames are determined. Second, a wavelength calibration is performed. Finally, the extraction of the intensity and/or polarization spectrum is performed by an optimal extraction method. Additionally, to eliminate any shifts in the spectrograph during an observing session, each wavelength calibrated spectrum is shifted to match the Least-Squared Deconvolved profile of the telluric lines contained in the spectrum. This reduces any instrumental shift to less than 0.1 km s^{-1}.

Frame Calibration (Geometric)

The geometrical elements of the raw echelle frames are extracted in a process which utilizes a flat field, an arc and a bias exposure. The frames are trimmed to remove

overscan and the frames may be mirrored to obtain a standard orientation with orders running vertically and wavelength increasing along with pixel number. The user provides an estimate of the location of the centre of the field and the width of the first order. The ESpRIT code then locates and traces each order in the flat-field frame.

Next, within each order, the spectrum of the arc frame is cross-correlated to trace the shape of the arc lines perpendicular to the dispersion. A linear or 2D quadratic fit to these measurements provides a measurement of the slit direction. The deviations from this mean slit direction averaged across all orders provides an estimate of the slit shape.

Frame Calibration (Wavelength)

Once the geometric characteristics of the raw frames are determined, the user provides an initial wavelength position and dispersion measurement for the first order. The ESpRIT code then attempts to calibrate the first selected order; starting with the initial user input and an atlas of known line positions, the code performs a preliminary identification of lines which should be present in the selected order. The code then iteratively calibrates each order. As Donati et al. (1997) mention, the code is very efficient, with mean rms calibration accuracies better than 0.3 pm (3 mÅ).

The calibration polynomials generated here are then used in the optimal extraction of the intensity and polarization spectra.

Extraction of Intensity Spectra

For the extraction of intensity spectra, ESpRIT requires the stellar exposure to be extracted, a flat-field exposure and a bias exposure in conjunction with the output of the

geometric and wavelength calibration processes described above. All frames are bias-subtracted and the stellar exposure is corrected for pixel-to-pixel sensitivity differences by dividing each pixel by the corresponding pixel in the flat-field exposure. An estimate of the inter-order background is obtained from the stellar exposure.

A preliminary spectrum is obtained by collapsing the orders along the slit direction and shape. At this point pixels which deviate too much from the average intensity of the order are excluded. This eliminates strong cosmic ray hits on the detector. The code then generates a false image by propagating the preliminary spectrum along the slit direction in each order, dividing by the actual stellar image. Marsh's (1989) scheme is then applied to give fractional fluxes as a function of the distance from the centre of the order. Finally, a new optimized spectrum is obtained.

The wavelength calibration is automatically corrected for the heliocentric motion of the observatory.

Extraction of Polarized Spectra

The extraction of polarized spectra is similar in principle to the intensity spectrum extraction. As mentioned in Section 3, observations in polarized light consist of a sequence of four stellar exposures, each of which contain two interleaving spectra corresponding to the orthogonal polarization states. The first and fourth exposures correspond to one position of the quarter-wave plate, the second and third corresponding to the second position. Each individual stellar exposure is processed as for an intensity spectrum, with both polarization states being extracted separately.

Once the four frames (yielding eight spectra) are processed, the mean intensity spectrum *I* is derived by adding the spectra. The polarization rate *P*/*I* is given by

$$\frac{P}{I} = \frac{R-1}{R+1} \qquad (2.1)$$

where

$$R^4 = \frac{i_{1,\perp} / i_{1,\parallel}}{i_{2,\perp} / i_{2,\parallel}} \frac{i_{4,\perp} / i_{4,\parallel}}{i_{3,\perp} / i_{3,\parallel}} \qquad (2.2)$$

$i_{k,\perp}$ and $i_{k,\parallel}$ being the two spectra obtained from the exposure *k*. The polarization is thus obtained by dividing spectra with orthogonal polarization states. This method eliminates systemic errors and spurious signals that result because both polarization states cannot be recorded at the same time on the same instrument.

A "null" polarization spectrum, *N*/*I* can be obtained be replacing *R* in equation (2.1) by

$$R^4 = \frac{i_{1,\perp} / i_{1,\parallel}}{i_{4,\perp} / i_{4,\parallel}} \frac{i_{2,\perp} / i_{2,\parallel}}{i_{3,\perp} / i_{3,\parallel}} \qquad (2.3)$$

This is interesting to check that the signature is in fact real. In the case that a cycle of four exposures is incomplete, a pair of exposures at different positions can still be used by replacing *R* in (2.1) by

$$R^2 = \frac{i_{1,\perp} / i_{1,\parallel}}{i_{2,\perp} / i_{2,\parallel}} \qquad (2.4)$$

although the null polarization can only be obtained from a full four-exposure cycle.

2.4 Analysis: Least Squares Deconvolution

The Zeeman magnetic signatures that we try to detect are very small; of the order of 0.1% of the relative amplitude. Even variations in the intensity profiles are small, although at ~ 1% of relative amplitude they are a factor of ten larger than the Zeeman signatures. In both cases, a high signal-to-noise ratio is required to accurately detect both phenomena. Donati et al. (1997) indicate that noise levels for the Stokes V profile must be of the order of 10^{-4}. This is not achievable with a single spectral line within a given spectrum. Also, co-adding spectra from different phases of the stellar rotation is not an option as the stars which we observe are rapid rotators and their activity varies on short timescales.

However, we assume the distortions due to spots (in intensity profiles) or magnetic fields (in Zeeman signatures) in spectral line profiles are the same across every spectral line in the entire spectrum.

Donati et al. (1997) present a technique called Least Squares Deconvolution (LSD) which we use to extract the intensity and magnetic information from many lines in a spectrum and combine them into a single, high-S/N line profile. In addition, due to the overlap in orders when taking echelle data, some spectral lines are seen twice, and the LSD technique takes advantage of these duplicate lines. (Note that some very strong lines such as Balmer lines and Na D are not used).

If the photospheric lines are all affected in the same way by the presence of spots or a magnetic field, then the observed profile of the lines is a convolution of a basic line pattern (M) and the spot signature (Z). The observed intensity profile (I) can thus be expressed as:

$$I = M * Z \qquad (2.5)$$

Similarly, the observed circularly polarized spectrum V can be expressed:

$$V = M * Z \qquad (2.6)$$

where M is a line mask. Masks of various stellar atmospheres from A0 to M0 have been computed using the Kurucz's atomic database (Kurucz, 1993).

Solving for Z by a least-squares method results in:

$$Z = ({}^{t}M \cdot S^{2} \cdot M)^{-1}\, {}^{t}M \cdot S^{2} \cdot I \qquad (2.7)$$

and

$$Z = ({}^{t}M \cdot S^{2} \cdot M)^{-1}\, {}^{t}M \cdot S^{2} \cdot V \qquad (2.8)$$

for intensity (2.7) and magnetic signature (2.8) respectively where S is a square diagonal matrix where S_{jj} is the inverse error bar ($1/\sigma_j$) for pixel j.

This deconvolves the raw cross-correlation function ($ {}^{t}M \cdot S^{2} \cdot I $, $ {}^{t}M \cdot S^{2} \cdot V $) from the autocorrelation profile matrix ($ {}^{t}M \cdot S^{2} \cdot M $) and provides a set of error bars for the mean intensity profile I and for the mean Zeeman signature (Z). The whole process is called Least Squares Deconvolution.

When using LSD for Zeeman Doppler Imaging (ZDI) data, a multiplex gain of up to 30 times in S/N can be obtained over the use of a single spectral line (Donati et al., 1997). While not quite as large, significant gains can also be obtained when using intensity profile (Doppler Imaging) data.

The LSD code, like the ESpRIT code used here is also provided by Jean-François Donati.

Magnetic Detection

The LSD code uses a reduced χ^2 statistical test to confirm the presence of a magnetic signal. The χ^2 test statistics are computed inside and outside the spectral lines for both the *V* and *N* (null) profiles, and converted into a detection probability. Generally, a signal is considered to be unambiguously detected in either *V* or *N* when the probability is calculated to be above 99.999%, or in other words when the computed "false alarm" probability is less than 10^{-5}. For a Zeeman signature to be considered a magnetic detection, the signal must be present in *V*, but not in *N*, and it must be located within the line profile velocity interval corresponding to:

$$(v_{\rm rad} - v \sin i) < v < (v_{\rm rad} + v \sin i)$$

where $v_{\rm rad}$ is the radial velocity of the star and $v \sin i$ the line-of-sight projected equatorial rotation rate.

2.5 Analysis: Maximum Entropy Image Reconstruction

By observing a star at different phases in its rotation, obtaining high-quality LSD profiles for both intensity and magnetic signatures, maximum entropy reconstruction is able to infer the surface topology of the star.

The imaging code used here is that of Brown et al. (1991) and Donati and Brown (1997) which implements the Skilling and Bryan (1984) algorithm for maximum entropy optimization. Maximum entropy reconstruction generates images which contain the minimum information (spot features or magnetic features) required to produce the observed spectroscopic variations.

The mapping of surface spot features uses the two-component brightness model from Cameron (1992) which reconstructs the local relative area occupied by cool spots for each pixel on the stellar surface. The "spot occupancy" varies from zero (no spot) to one (maximum spottedness). LSD profiles of slowly-rotating stars are used as the templates for describing the contribution of the photosphere and spot, as described in Donati and Cameron (1997). A linear limb-darkening law is used to simulate the variations of the continuum intensity over the stellar disc.

In the Doppler Imaging code, the form of entropy used is

$$S[f,m] = S_1[f,m] + S_1[(1-f),(1-m)] \qquad (2.9)$$

where

$$S_1[f,m] = \sum_i \; [f_i(\log(\frac{f_i}{m_i} - 1) + m_i] \qquad (2.10)$$

and

$$S_1[(1-f),(1-m)] = \sum_i [(1-f_i)(\log(\frac{(1-f_i)}{(1-m_i)} - 1) + (1-m_i)] \qquad (2.11)$$

In these equations, f is the photosphere filling factor ($0 < f < 1$, where 0 is total spot, 1 no spot). When presenting the resulting Doppler Imaging maps, however, 0 represents no spot, and 1 represents a total spot. m is the default unspotted filling factor (set to 0.9999).

The values for the filling factors are then adjusted to maximize:

$$Q = S(f,m) - \lambda\chi^2(f,m) \qquad (2.12)$$

where λ is the Lagrange multiplier and $\chi^2(f,m)$ measures the accuracy of the fit. This is determined by:

$$\chi^2(f,m) = \sum_k \left(\frac{F_k - D_k}{\sigma_k}\right)^2 \qquad (2.13)$$

where F_k is the modeled data, D_k is the observed data and σ_k is calculated from an estimate in the Least Squares Deconvolution profiles. The data are then fitted to within a desired accuracy of $\chi^2 = \chi^2_{\text{aim}}$. Ordinarily, χ^2_{aim} is set to one; that is the data are fitted to the noise level. If $\chi^2_{\text{aim}} < 1$ is achieved, then this means that the error bars have been overestimated. However, this has no effect on the images derived by the code.

For magnetic tomographic imaging, the model described by Donati and Brown (1997) is used. This assumes weak magnetic fields and a constant Gaussian intrinsic profile over the stellar surface. The method used by Donati and Brown (1997) results in three images which correspond to the radial, meridional and azimuthal components of the stellar magnetic field. However, the code is essentially the same as described for surface spot tomography.

Chapter 3

Results and Discussion

3.1 Results: Magnetic Field Detection on HR 1817

An initial investigation of the F7 dwarf HR 1817 was attempted on the night of December 9, 2000 with the instrumental setup described in Chapter 2. As shown in the log of observations in Table 2.1, 16 observations comprising four complete cycles of polarization observations were obtained.

ESpRIT was used to reduce the data, and Least Squares Deconvolution was used to generate the mean intensity profiles and magnetic signatures for each of the 4 cycles. In each case, over 2000 spectral lines were used in the calculation. The signal-to-noise parameters for each cycle are shown in Table 3.1, and the Least Squares Deconvolved line profiles are plotted in Figure 3.1.

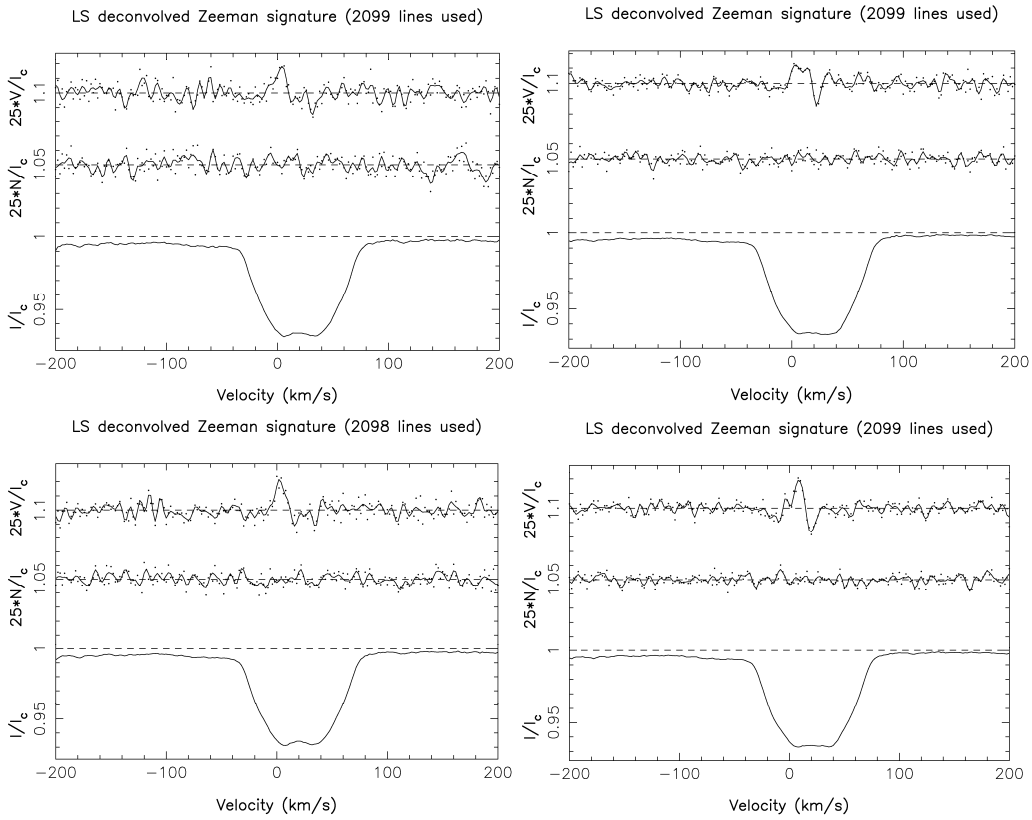

Figure 3.1 Detection of magnetic field on HR 1817, December 9, 2000. Start Times: top left UT 09:55; bottom left UT 10:20; top right UT 11:10; bottom right UT 11:40. The top line in each frame is the Stokes V profile (magnetic signature), the central line the null polarization profile, and the lower line the Stokes I (intensity) profile. In each, the magnetic signature indicates the presence of magnetic features, although the analysis program claims no detection in the top left frame. The N and V profiles have been multiplied by 25 and shifted upwards for clarity. They are smoothed fits (3 pixel) to the actual data shown as points.

Table 3.1 Observations from December 9, 2000. The total exposure time in column 4 is the cumulative time over the cycle of 4 exposures. The measurement of S/N is the peak signal-to-noise ratio per pixel of 1.9 km s^{-1} for the Stokes I and Stokes V measurements. S/N_{LSD} is the signal-to-noise ratio in the associated Stokes I and Stokes V deconvolved spectra. The multiplex gain for each Stokes I and Stokes V is shown. Note that as mentioned, the multiplex gain for Stokes V is much greater than that for Stokes I.

Polarization Cycle	UT Start	Stellar Exposures	Total Exposure Time (s)	S/N		S/N_{LSD}		Multiplex Gain	
				I	V	I	V	I	V
1	09:55:36.68	21,22,23,24	1200	200	190	916	4144	4.6	21.8
2	10:20:23.93	25,26,27,28	1200	240	230	944	4832	3.9	21.0
3	11:10:30.25	33,34,35,36	1200	320	310	986	7189	3.1	23.2
4	11:35:11.58	37,38,39,40	1200	280	280	992	6514	3.5	23.3

The LSD analysis statistical tests produced no detection in the first observational cycle. The detection probability was 0.9863, which while high, was outside the parameters set to classify a detection. The null polarization profile in the image suggests that the noise was relatively high and as such any signal which may be there (and indeed upon visual inspection, there appears to be a signal) is not sufficiently strong to be classified as definitely detected.

In cycles 2, 3 and 4, the analysis produced definite magnetic detections with detection probabilities of 1.000 in each case. The false alarm probabilities in the respective cycles were 1.514×10^{-8}, zero, and 7.007×10^{-8}.

The shape of the Stokes I profile in each case is indicative of spottedness, and in particular exhibits the "flat bottom" characteristic of many other stars which show both a similar profile and polar spots.

In the case of both the Stokes I and Stokes V profiles, evolution in the shape of the profiles is evident within the relatively short (~ 2 hours) period of the observations. This is likely to be caused by rotational modulation: the rotation of the star causing the transit of active areas across its visible disc.

This confirmation of the magnetic activity of HR 1817 and the possibility of rotationally modulated features made HR 1817 an attractive target for further investigation with Doppler and Zeeman Doppler Imaging.

Initial Estimate of Radial Velocity

A valuable property which can be derived from the Stokes I profile is the stellar radial velocity. The entire profile is offset from 0 km s^{-1} by an amount equivalent to the radial

velocity. The radial velocity of HR 1817 is found to be approximately 21 km s^{-1}. A χ^2 minimization technique is used in Section 3.5 to refine the redial velocity of HR 1817.

3.2 Results: Doppler Imaging of HR 1817

A fundamental problem arose when attempting to perform Doppler Imaging of HR 1817. HR 1817 rotates in almost exactly one day. This meant that despite observing the star over four nights which spanned over ten rotational periods of the star, each night only the same third of the star was observed. This means that the mapping process can only recover those areas of the stellar surface which are observed.

The stellar inclination angle is assumed to be 50°, derived from

$$\sin i = \frac{P \cdot v \sin i}{2\pi R} \qquad (3.1)$$

given that the $v \sin i$ is 50 km s^{-1}, the rotation period, P is 1 day, and R is 1.18 $R_{\odot}$. This result is confirmed by a χ^2 minimization technique shown in Section 3.5.

December 23, 2001

The first night of observation of HR 1817 was December 23, 2001. A total of 31 stellar exposures were taken. Optimal extraction and Least Squares Deconvolution was performed on each frame. Due to weather effects, observations were only possible at the start and end of the night. Consequently less than 10% phase coverage was possible, and the phase coverage was split into two sections separated by a large gap. Figure 3.2 shows the maximum entropy fits to the observed LSD profile with a χ^2_{aim} of 0.5.

The reconstructed image, shown in Figure 3.3 exhibits a small polar spot (relative to those observed in G and K dwarfs. There are two faint mid-latitude features visible, however they appear elongated and distorted due to the paucity of phase coverage. Overall spot coverage is 0.018 (or 1.8%), again much lower than that in G and K dwarfs imaged in this way.

December 26, 2001

On December 26, 2001, a much more comprehensive phase coverage was obtained, with 76 stellar exposures. All frames were extracted and LSD performed. Figure 3.4 shows the maximum entropy fits to the observed profiles with a χ^2_{aim} of 0.35. Figure 3.5 presents the reconstructed spot occupancy image for December 26.

The much higher phase coverage reveals more detail in the mid-latitude features. At least six spots are clearly visible between latitudes +30° and +60°. The polar spot is still clearly visible. The spot coverage is 0.021 (2.1%).

December 30, 2001

The third night of observations, 65 stellar frames of HR 1817 were obtained. All frames were extracted and LSD performed. Figure 3.6 shows the maximum entropy fits to the observed profiles with a χ^2_{aim} of 0.35. Figure 3.7 shows the reconstructed spot occupancy image for December 30. While the basic features are shown, there is a lack of resolution, possibly due to a slightly higher noise level, and a slightly reduced phase coverage from the previous observing night. Spot coverage for December 30 was 0.020 (2.0%).

January 2, 2002

During the final night of observations only a small phase coverage of 32 exposures early in the night was possible. Consequently, much of the detail seen on the previous nights was not resolved.

All frames were extracted and LSD performed. Figure 3.8 shows the maximum entropy fits to the observed profiles with a χ^2_{aim} of 0.5. Figure 3.9 shows the reconstructed spot occupancy image for January 2. Spot coverage for January 2 was 0.014 (1.4%), again due to the lack of phase coverage.

Comparison of Nights

As the phase coverage of HR 1817 was only about one third, the above measurements of spot coverage must be treated as lower limits, given that two-thirds of the star is not visible. Even in the individual nightly observations, higher phase coverage results in slightly higher observed spot coverage in the reconstructed images due to the increased fraction of the star being observed. Hussain (1999) also indicates that poor phase coverage leads to a loss of information in some of the reconstructed features.

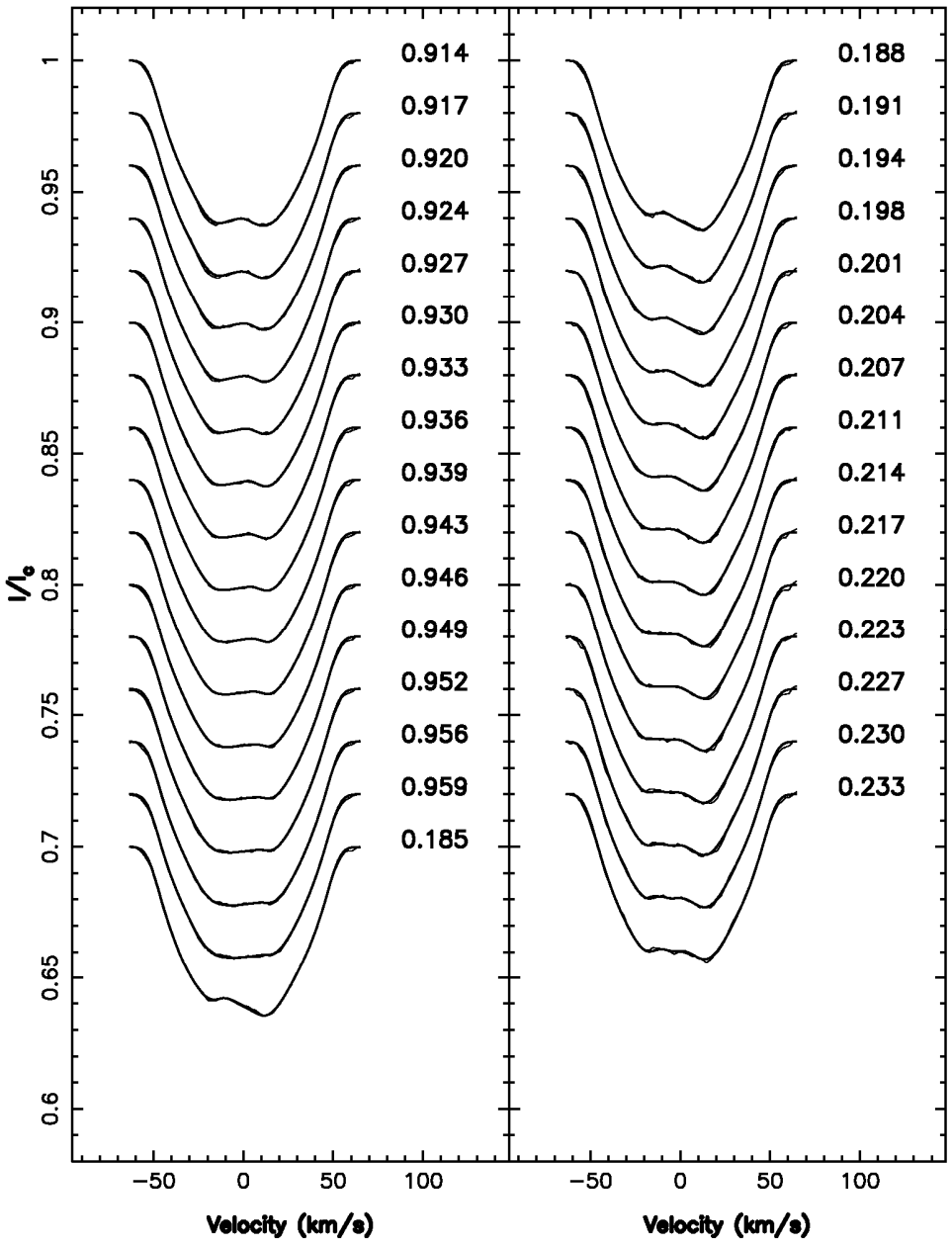

Figure 3.2 Maximum entropy fits to the LSD Stokes I profiles of HR 1817 for December 23, 2001. The thin lines are the observed profiles, the thick lines are the fits produced by the Doppler Imaging Code. Each successive image is shifted for graphical purposes. The fits are equivalent to χ^2_{aim} of 0.5. The number to the right of each profile is the rotational phase of the observation.

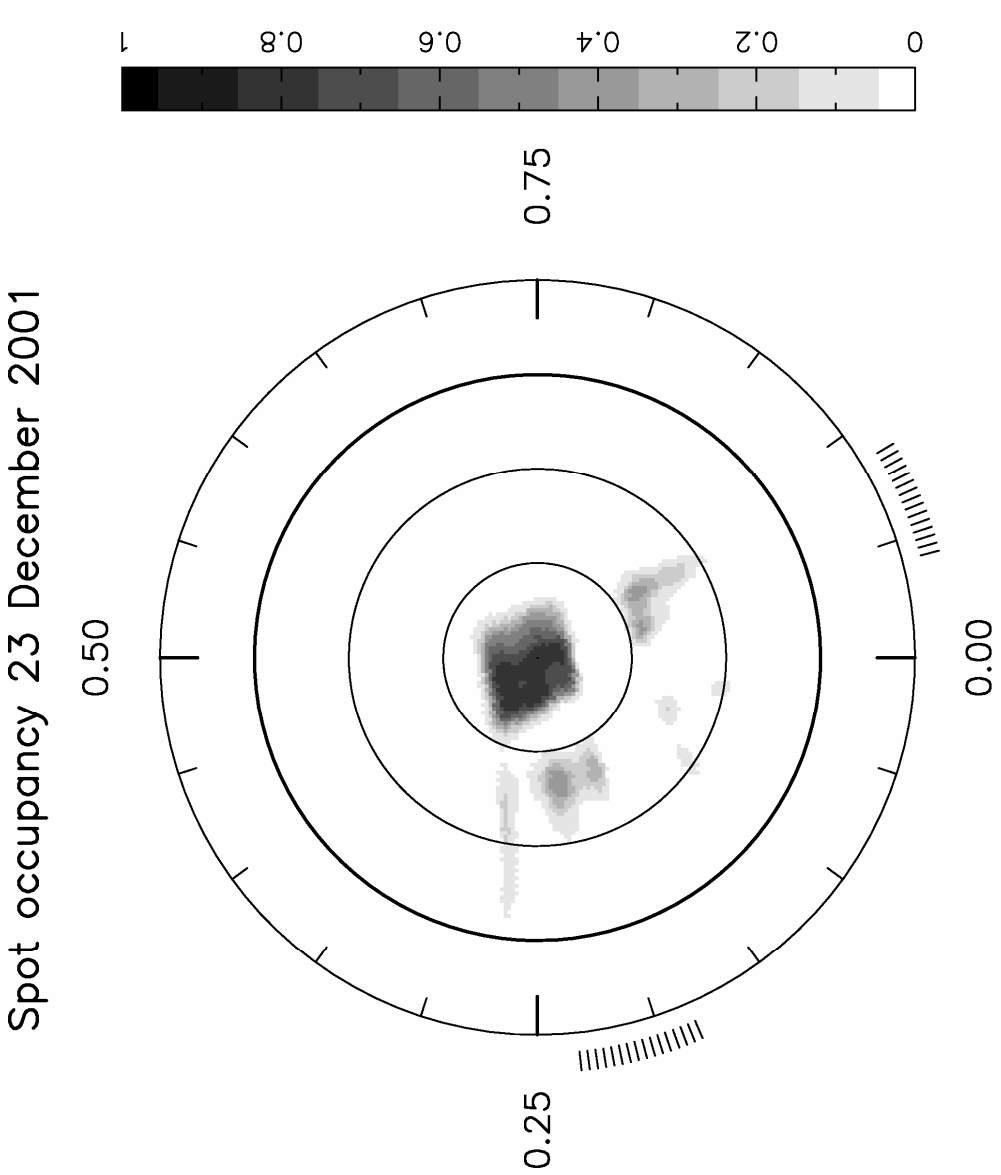

Figure 3.3 Maximum entropy brightness image for 23 December, 2001. The image is a flattened polar projection extending down to a latitude of -30°. The radial ticks outside the plot indicate the phases at which observations were taken. The χ^2_{aim} was 0.5 and the spot occupancy is 0.018 (1.8%). Note the polar spot. The coverage of the star is sparse, and hence the resolution is consequently coarse, resulting in the elongation of the mid-latitude features.

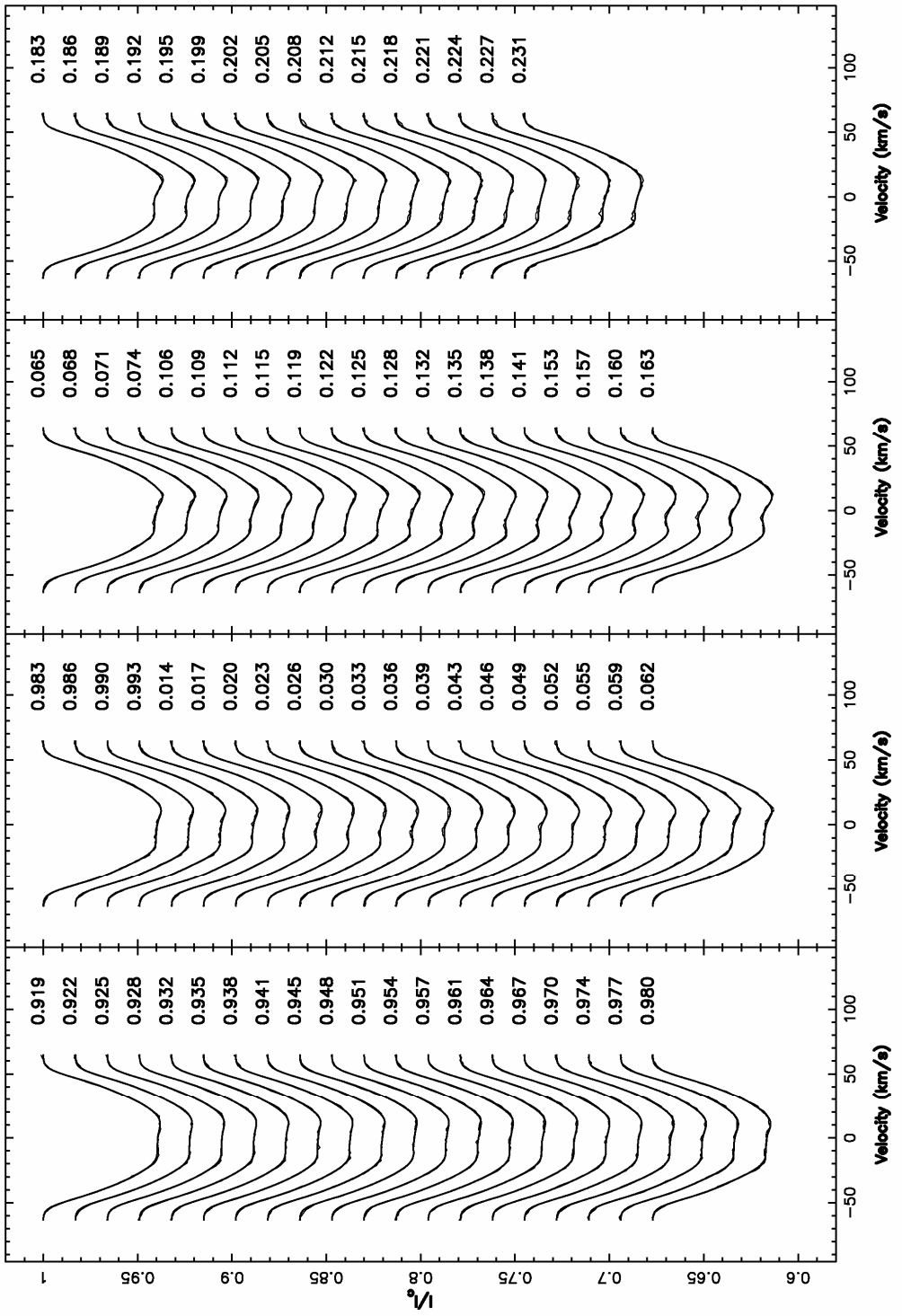

Figure 3.4 Maximum entropy fits to the LSD Stokes I profiles of HR 1817 for December 26, 2001. The thin lines are the observed profiles, the thick lines are the fits produced by the Doppler Imaging Code. Each successive image is shifted for graphical purposes. The fits are equivalent to $\chi^2_{\rm aim}$ of 0.35. The number to the right of each profile is the rotational phase of the observation.

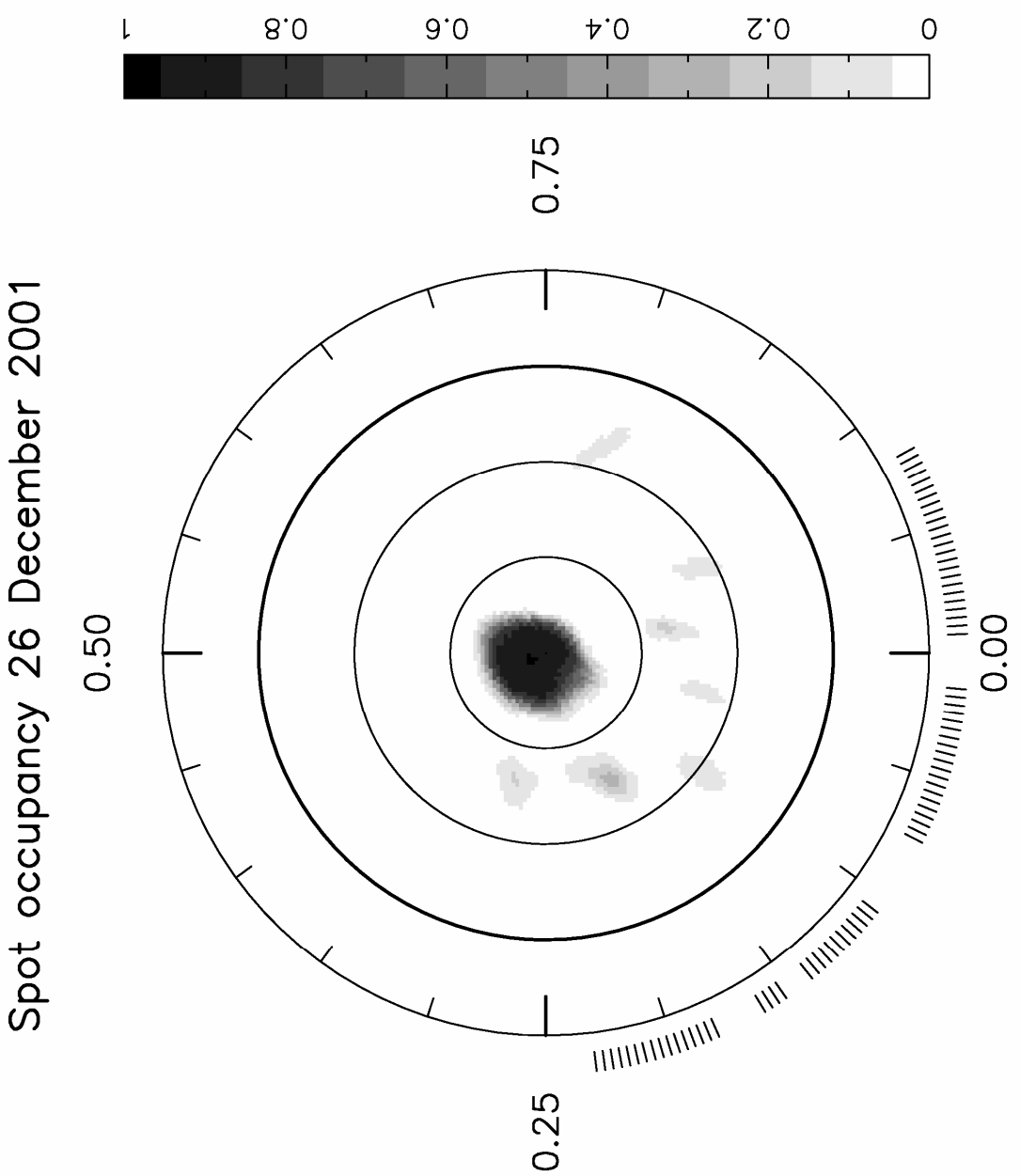

Figure 3.5 Maximum entropy brightness image for 26 December, 2001. The image is a flattened polar projection extending down to a latitude of -30°. The radial ticks outside the plot indicate the phases at which observations were taken. The χ^2_{aim} was 0.5 and the spot occupancy is 0.021 (2.1%). The phase coverage is much higher than the previous night. Note the presence of weak mid-latitude features.

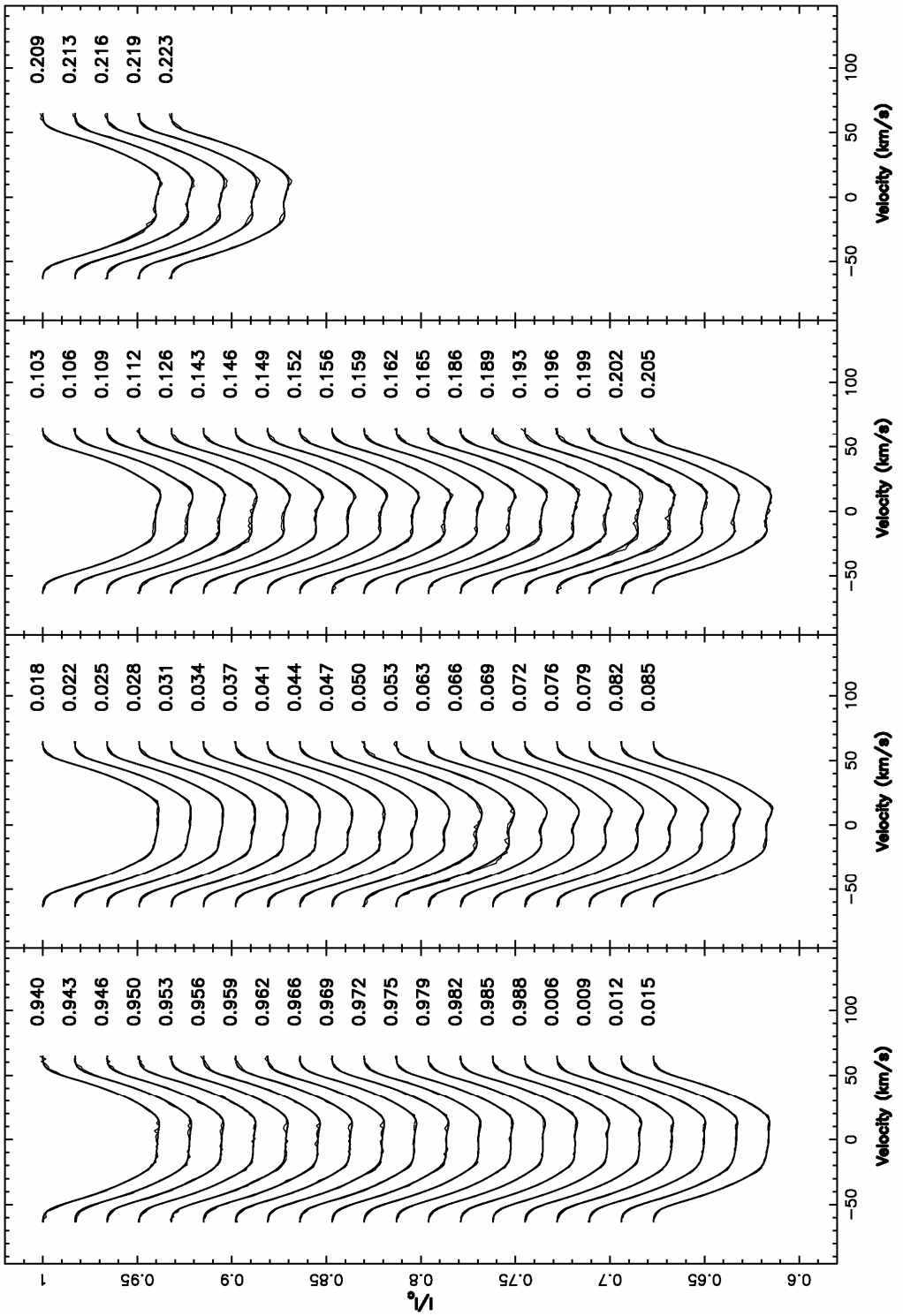

Figure 3.6 Maximum entropy fits to the LSD Stokes I profiles of HR 1817 for December 30, 2001. The thin lines are the observed profiles, the thick lines are the fits produced by the Doppler Imaging Code. Each successive image is shifted for graphical purposes. The fits are equivalent to χ^2_{aim} of 0.35. The number to the right of each profile is the rotational phase of the observation.

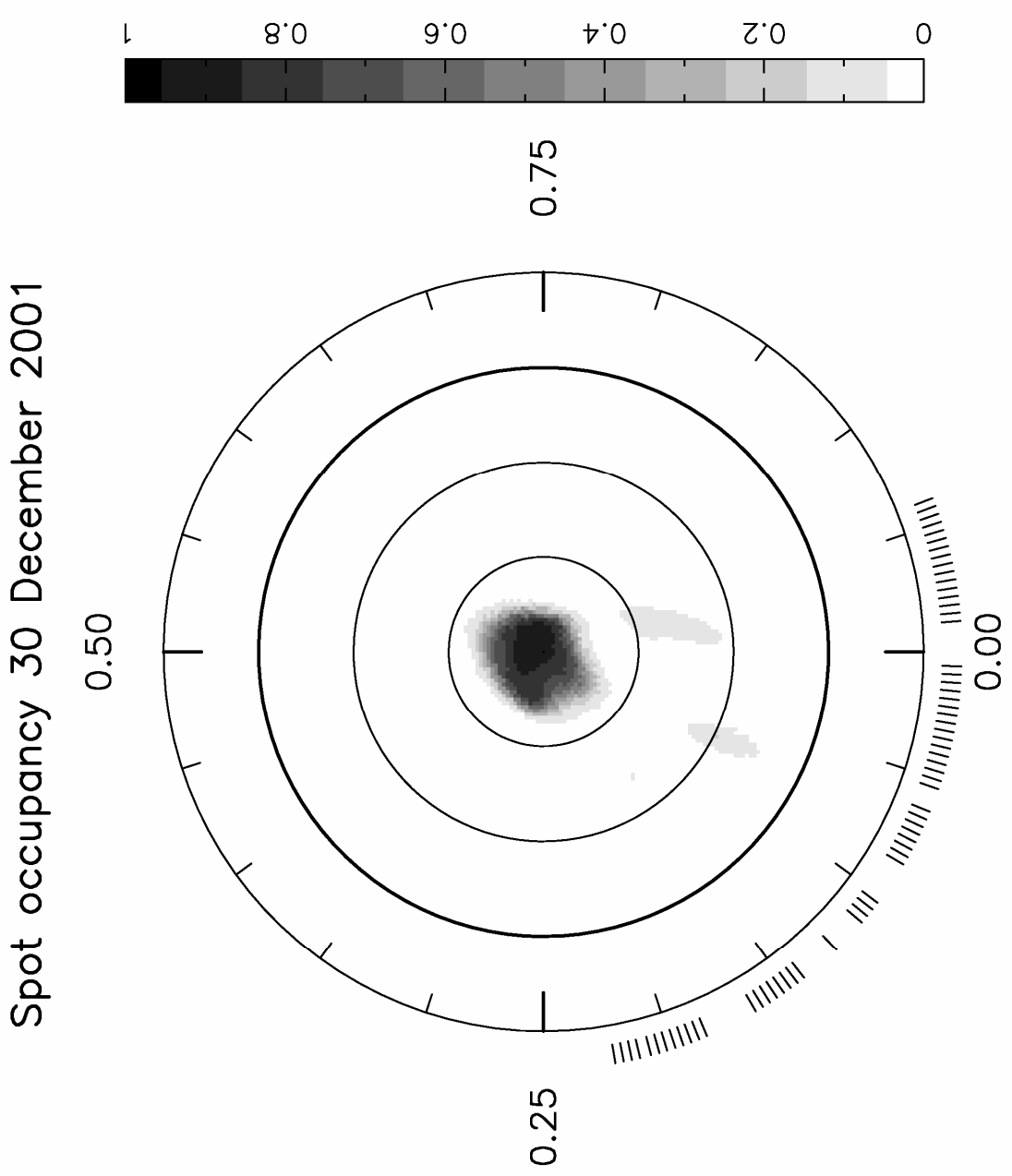

Figure 3.7 Maximum entropy brightness image for 30 December, 2001. The image is a flattened polar projection extending down to a latitude of -30°. The radial ticks outside the plot indicate the phases at which observations were taken. The χ^2_{aim} was 0.5 and the spot occupancy is 0.020 (2.0%).

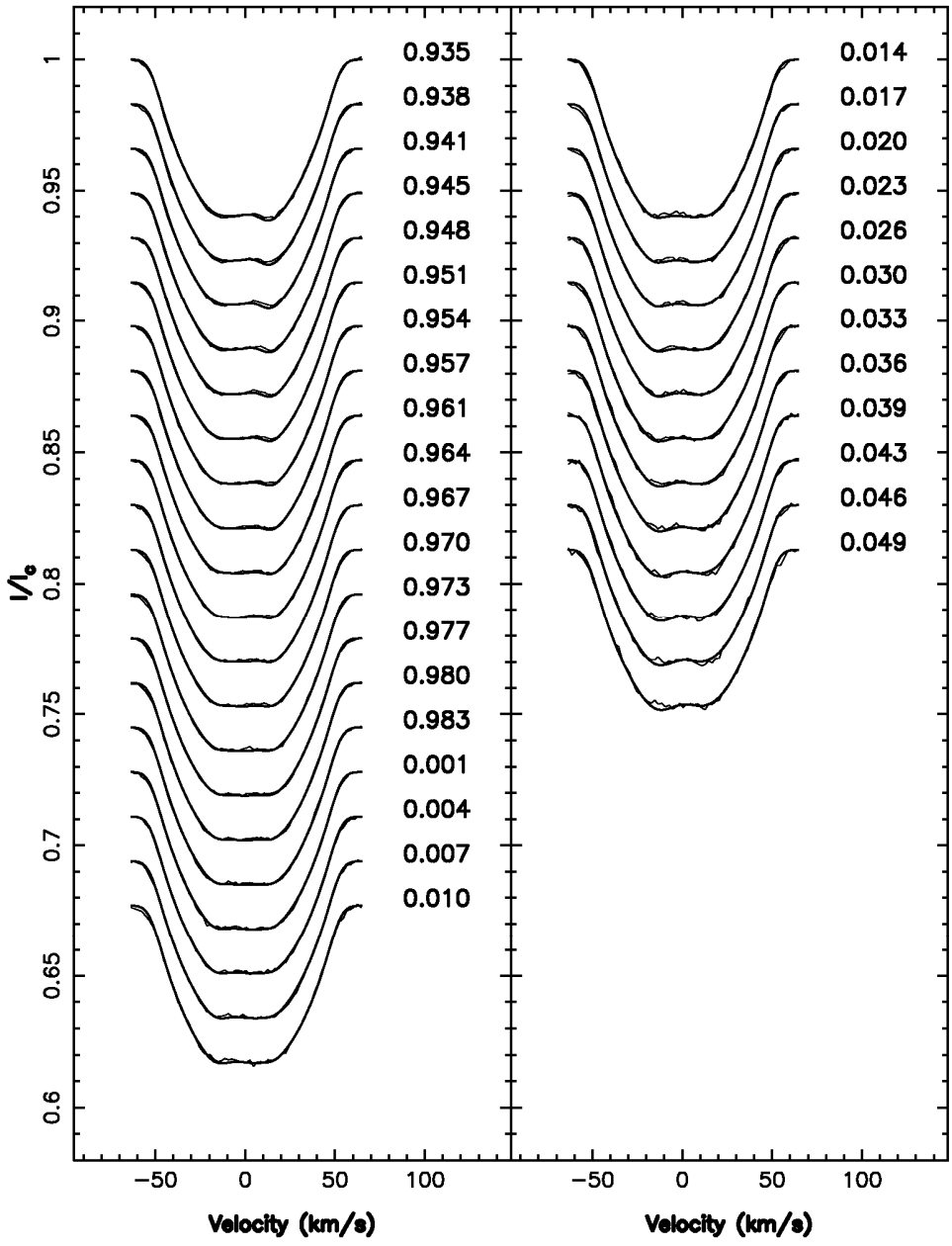

Figure 3.8 Maximum entropy fits to the LSD Stokes I profiles of HR 1817 for January 2, 2002. The thin lines are the observed profiles, the thick lines are the fits produced by the Doppler Imaging Code. Each successive image is shifted for graphical purposes. The fits are equivalent to χ^2_{aim} of 0.5. The number to the right of each profile is the rotational phase of the observation.

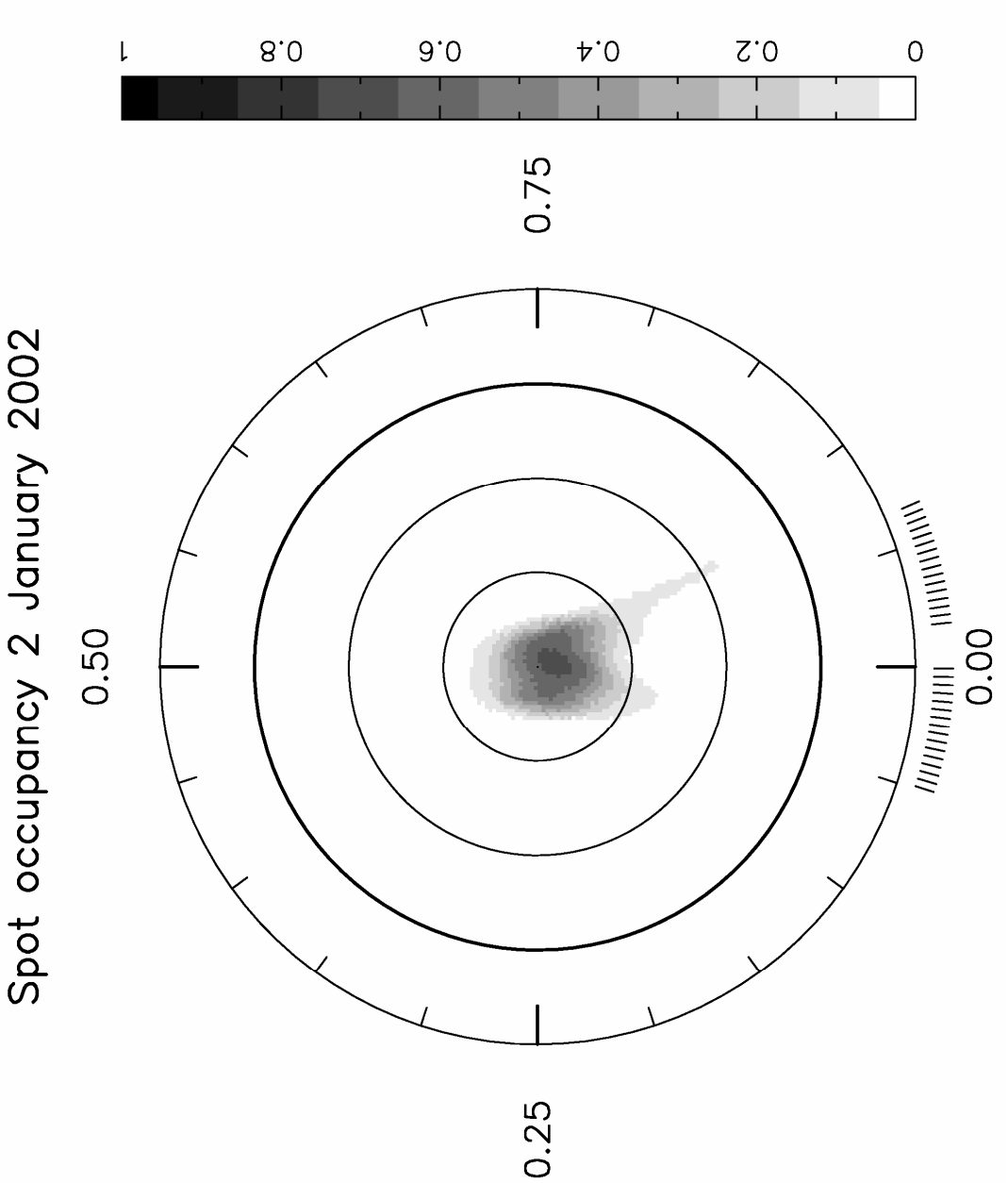

Figure 3.9 Maximum entropy brightness image for 2 January, 2002. The image is a flattened polar projection extending down to a latitude of -30°. The radial ticks outside the plot indicate the phases at which observations were taken. The χ^2_{aim} was 0.5 and the spot occupancy is 0.014 (1.4%). The coverage of the star is sparse, resulting in the non-appearance of features present in other reconstructed images.

Combined Image

By combining the data for all four nights, a definitive map of the surface brightness of HR 1817 can be derived. All 204 images take over the four nights of observation were processed, and the Doppler Imaging code applied with a χ^2_{aim} of 0.35. This low χ^2_{aim} reflects the high quality of the data in terms of S/N level and the resulting ability of the model to fit the data. Differential rotation was taken into account using parameters derived in the processes described in Sections 3.4 and 3.5. Figures 3.10a and 3.10b show the maximum entropy fits to the observed profiles for the combined data set. Figure 3.11 shows the reconstructed image, taking into account differential rotation and using all observations. (The nightly images did not take into account differential rotation). Figure 3.12 shows a spherical projection of the same reconstructed image as in the flattened polar projection of Figure 3.11.

The combined image shows the prominent polar spot, and a number of weak mid-latitude features. The total spot coverage is 0.020, or 2.0% of the stellar disc.

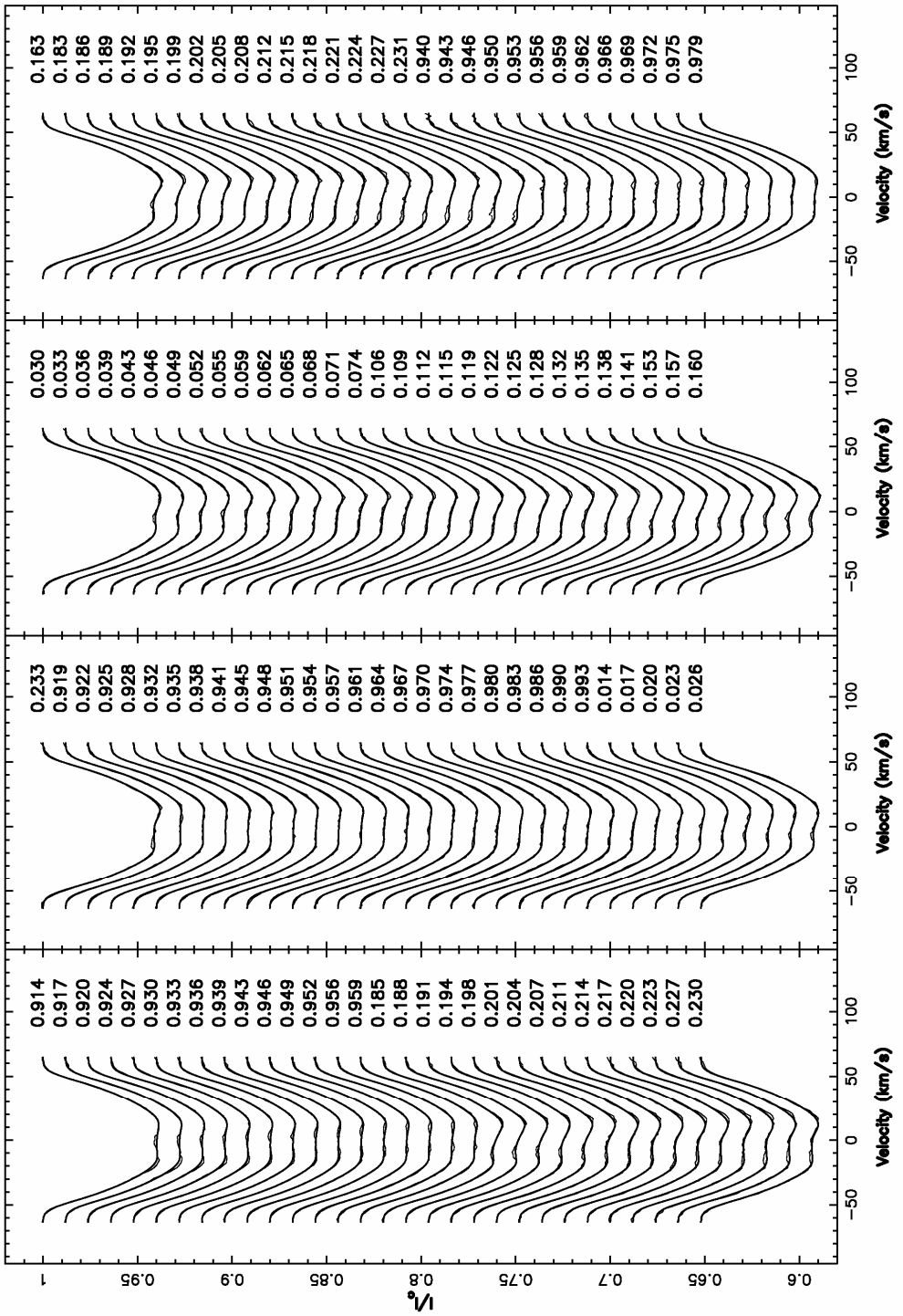

Figure 3.10 (a) Maximum entropy fits to the LSD Stokes I profiles of HR 1817 for all exposures. The thin lines are the observed profiles, the thick lines are the fits produced by the Doppler Imaging Code. Each successive image is shifted for graphical purposes. The fits are equivalent to χ^2_{aim} of 0.35. The number to the right of each profile is the rotational phase of the observation.

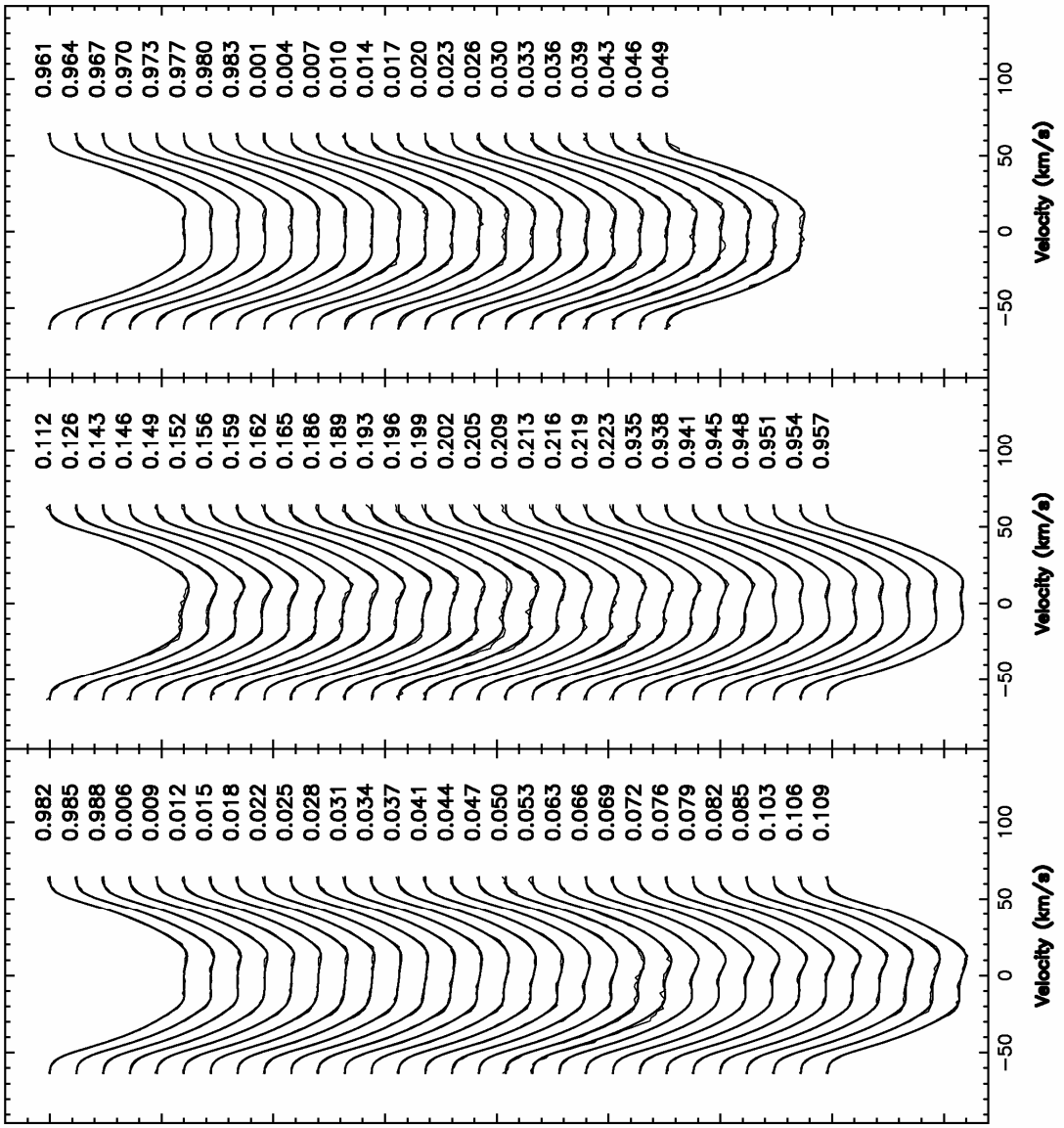

Figure 3.10 (b) Maximum entropy fits to the LSD Stokes I profiles of HR 1817 for all exposures. The thin lines are the observed profiles, the thick lines are the fits produced by the Doppler Imaging Code. Each successive image is shifted for graphical purposes. The fits are equivalent to χ^2_{aim} of 0.35. The number to the right of each profile is the rotational phase of the observation.

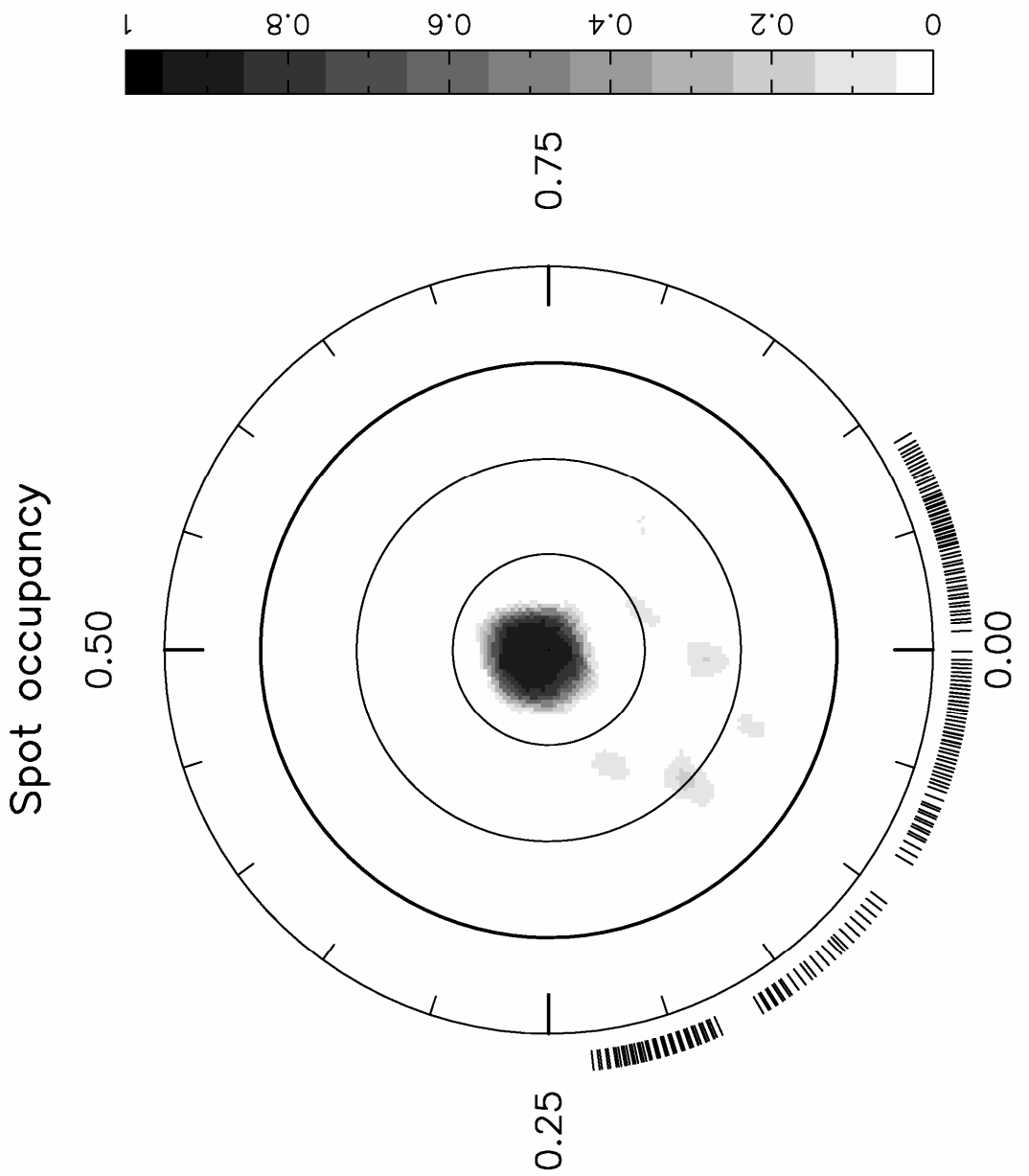

Figure 3.11 Maximum entropy brightness image for all data sets combined. The image is a flattened polar projection extending down to a latitude of -30°. The radial ticks outside the plot indicate the phases at which observations were taken. The χ^2_{aim} was 0.35 and the spot occupancy 0.020 (2.0%).

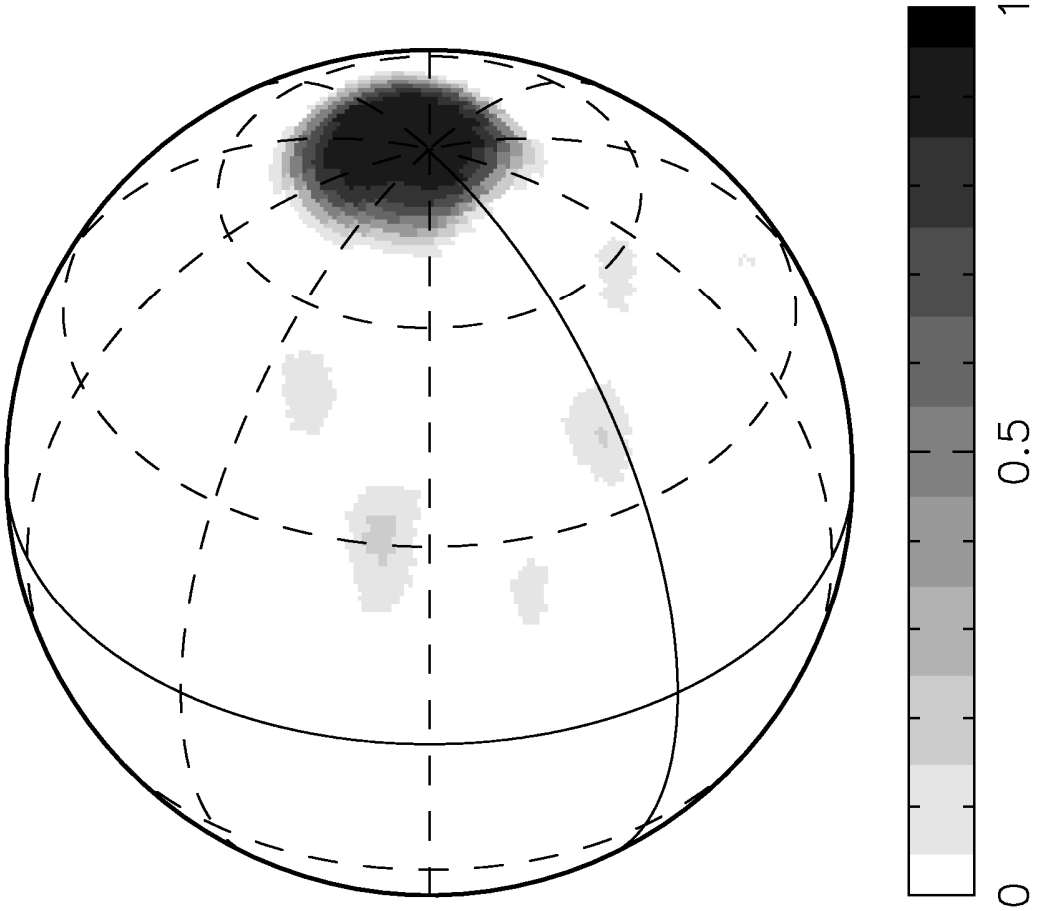

Figure 3.12 Maximum entropy brightness image for all data sets combined. The image presents the same data as Figure 3.11, but is a spherical projection, centred on phase 0.1. The $\chi^2_{\rm aim}$ was 0.35 and the spot occupancy 0.020 (2.0%).

3.3 Results: Zeeman Doppler Imaging of HR 1817

Zeeman Doppler Imaging (ZDI) produces a map illustrating the magnetic tomography of the star. Not only does ZDI show the position of magnetic regions, but also the orientation of the magnetic features. ZDI of the F7 dwarf HR 1817 was attempted over the four nights of December 23, 26 and 30, 2001 and January 2, 2002 with the instrumental setup described in Section 3. Fifty observations comprising four complete cycles of polarization observations were taken across the four nights and one partial cycle of two observations.

ESpRIT was used to reduce the data, and Least Squares Deconvolution was used to generate the mean magnetic signatures for each of the 51 cycles. In each case, over 2000 spectral lines were used in the calculations. The signal-to-noise parameters for each cycle are shown in Table 3.2. The resulting Stokes V profiles are shown in figure 3.13. The ZDI code was then applied to the Stokes V profiles. All 51 cycles were used, and differential rotation was taken into account using the parameters derived in Sections 3.4 and 3.5. Figure 3.13 shows the maximum entropy fits to the observed profiles. A χ^2_{aim} of 1.0 was used.

The resulting reconstructed maps are shown in Figure 3.14. A map is generated for each of the radial, azimuthal and meridional components of the magnetic field. Figures 3.14 (polar projection) and 3.15 (spherical projection) show that the meridional component of the magnetic field is almost non-existent. The azimuthal component of the field appears to be a unipolar ring above +60° latitude. The radial component of the field is weaker than that observed on many G and K dwarfs, but exhibits a rich structure of many small bipolar features at mid-latitudes between +30° and +60°. Hussain (1999)

states that poor phase coverage leads to the strength of the reconstructed flux being suppressed. Thus the reconstructed magnetic topology of HR 1817 represents a lower limit of the flux given that two-thirds of the stellar surface was not observed.

Table 3.2 Table of polarization observations. Each polarization observation is a cycle of four exposures (except observation 4, which is two) of alternating polarization positions (P1-P2-P2-P1). The numbers in the column "Stellar Exposures" corresponds to the exposure numbers in Table 2.2. The measurement of S/N is the peak signal-to-noise ratio per pixel of 1.7 km s^{-1} for the Stokes I and Stokes V measurements. S/N_{LSD} is the signal-to-noise ratio in the associated Stokes I and Stokes V deconvolved spectra. The multiplex gain for each Stokes I and Stokes V is shown.

Polarization Cycle	UT Start	Stellar Exposures	Total Exposure Time (s)	S/N		S/N_{LSD}		Multiplex Gain	
December 23, 2001				I	V	I	V	I	V
1	09:54:16.97	24,25,26,27	800	270	280	977	8275	3.6	29.6
2	10:12:49.48	28,29,30,31	800	280	300	983	8549	3.5	28.5
3	10:31:12.63	32,33,34,35	800	270	280	988	8463	3.7	30.2
4	10:49:46.96	36,37	400	190	190	981	5885	5.2	31.0
5	16:24:43.52	47,48,49,50	800	230	240	977	6863	4.2	28.6
6	16:43:27.30	51,52,53,54	800	200	210	963	5911	4.8	28.1
7	17:01:49.64	55,56,57,58	800	170	170	946	4987	5.6	29.3
8	17:20:17.27	59,60,61,62	800	200	200	921	5257	4.6	26.3
December 26, 2001									
9	10:01:33.64	29,30,31,32	800	200	200	1040	6868	5.2	34.3
10	10:20:11.51	33,34,35,36	800	190	200	1042	6502	5.5	32.5
11	10:38:36.57	37,38,39,40	800	180	200	1044	6299	5.8	31.5
12	10:57:09.06	41,42,43,44	800	170	180	1041	5912	6.1	32.8
13	11:15:41.00	45,46,47,48	800	170	180	1043	5820	6.1	32.3
14	11:34:05.26	49,50,51,52	800	170	180	1042	5702	6.1	31.7
15	12:18:06.72	57,58,59,60	800	200	220	1047	6476	5.2	29.4
16	12:36:29.14	61,62,63,64	800	200	210	1044	6509	5.2	31.0
17	12:55:03.73	65,66,67,68	800	190	200	1045	6180	5.5	30.9
18	13:13:26.32	69,70,71,72	800	200	200	1045	6295	5.2	31.5
19	13:31:53.15	73,74,75,76	800	210	220	1043	6500	5.0	29.5
20	14:30:56.93	81,82,83,84	800	210	220	1044	6586	5.0	29.9
21	14:49:21.83	85,86,87,88	800	210	220	1041	6474	5.0	29.4
22	15:07:44.72	89,90,91,92	800	220	220	1035	6609	4.7	30.0
23	15:39:14.36	93,94,95,96	800	210	210	1031	6036	4.9	28.7
24	16:21:18.86	101,102,103,104	800	200	210	1011	5681	5.1	27.1
25	16:39:42.29	105,106,107,108	800	190	200	1000	5217	5.3	26.1
26	16:58:05.76	109,110,111,112	800	190	200	985	4858	5.2	24.3
27	17:16:50.02	113,114,115,116	800	170	180	963	4345	5.7	24.1
December 30, 2001									
28	10:32:09.98	33,34,35,36	800	120	120	983	3724	8.2	31.0
29	10:50:37.12	37,38,39,40	800	140	150	995	4383	7.1	29.2

Table 3.2 (continued)

Polarization Cycle	UT Start	Stellar Exposures	Total Exposure Time (s)	S/N		S/N_{LSD}		Multiplex Gain	
December 30, 2001									
				I	V	I	V	I	V
30	11:09:06.50	41,42,43,44	800	220	220	1010	6926	4.6	31.5
31	11:27:36.60	45,46,47,48	800	280	290	1015	8885	3.6	30.6
32	12:06:23.58	53,54,55,56	800	300	320	1016	9510	3.4	29.7
33	12:24:45.92	57,58,59,60	800	290	300	1019	9346	3.5	31.2
34	12:43:14.83	61,62,63,64	800	260	270	1018	8455	3.9	31.3
35	13:01:36.29	65,66,67,68	800	150	120	1007	3980	6.7	33.2
36	13:28:40.44	69,70,71,72	800	310	320	1017	10058	3.3	31.4
37	13:47:04.55	73,74,75,76	800	310	330	1018	10331	3.3	31.3
38	14:26:21.06	81,82,83,84	800	200	170	1007	5369	5.0	31.6
39	15:24:09.07	86,87,88,89	800	200	200	991	6082	5.0	30.4
40	15:42:33.26	90,91,92,93	800	170	170	973	5017	5.7	29.5
41	16:26:25.43	98,99,100,101	800	150	110	941	3115	6.3	28.3
42	16:44:49.70	102,103,104,105	800	160	150	914	4529	5.7	30.2
43	17:04:59.40	106,107,108,109	800	200	200	886	5705	4.4	28.5
January 2, 2002									
44	10:24:46.46	24,25,26,27	800	240	250	986	7829	4.1	31.3
45	10:43:11.04	28,29,30,31	800	230	240	983	7466	4.3	31.1
46	11:01:45.79	32,33,34,35	800	220	240	989	7494	4.5	31.2
47	11:20:10.79	36,37,38,39	800	200	200	987	6322	4.9	31.6
48	11:59:26.43	44,45,46,47	800	150	160	988	4781	6.6	29.9
49	12:17:57.82	48,49,50,51	800	120	120	982	3818	8.2	31.8
50	12:36:28.82	52,53,54,55	800	110	110	973	3343	8.8	30.4
51	12:54:56.45	56,57,58,59	800	95	99	959	2849	10.1	28.8

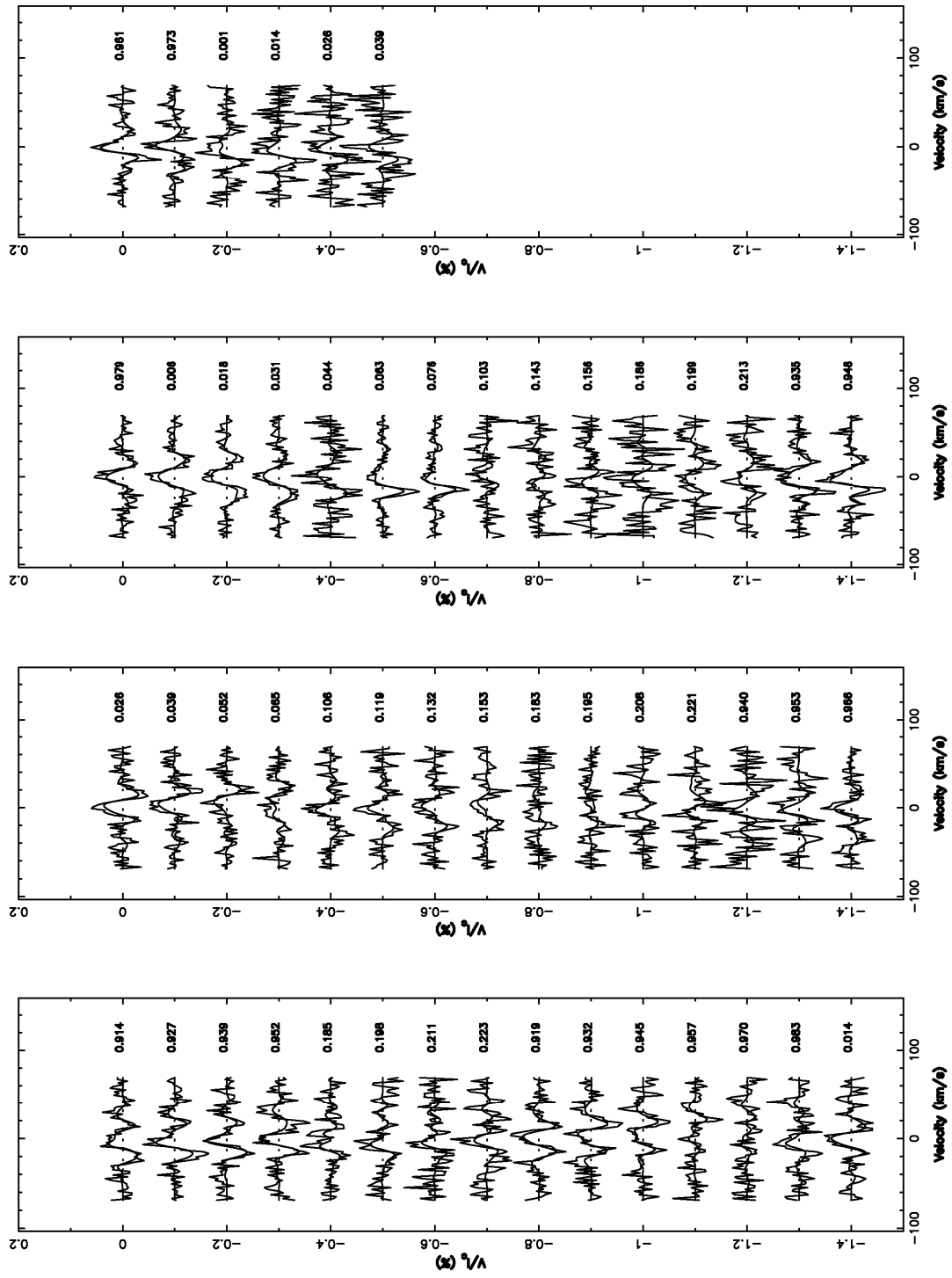

Figure 3.13 Maximum entropy fit (thick line) to the observed Stokes V profiles (thin line). The dotted line in each is the zero circular polarization level of each profile. The number to the right of each profile is the rotational phase of each observation.

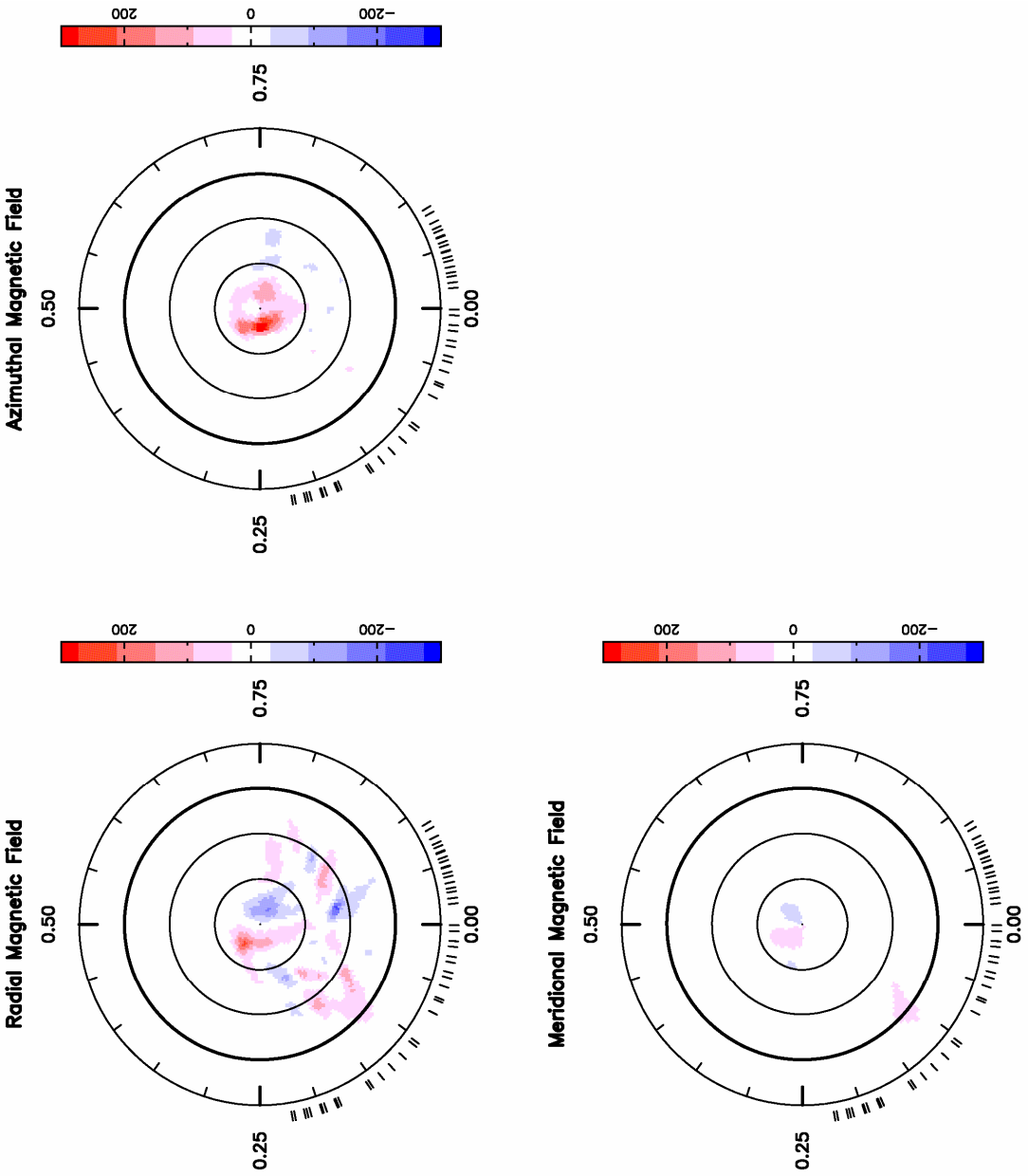

Figure 3.14 Maximum entropy reconstructed magnetic maps of HR 1817. These are based on all observations across the four nights. The radial ticks outside the plots show the rotational phases when observations were taken.

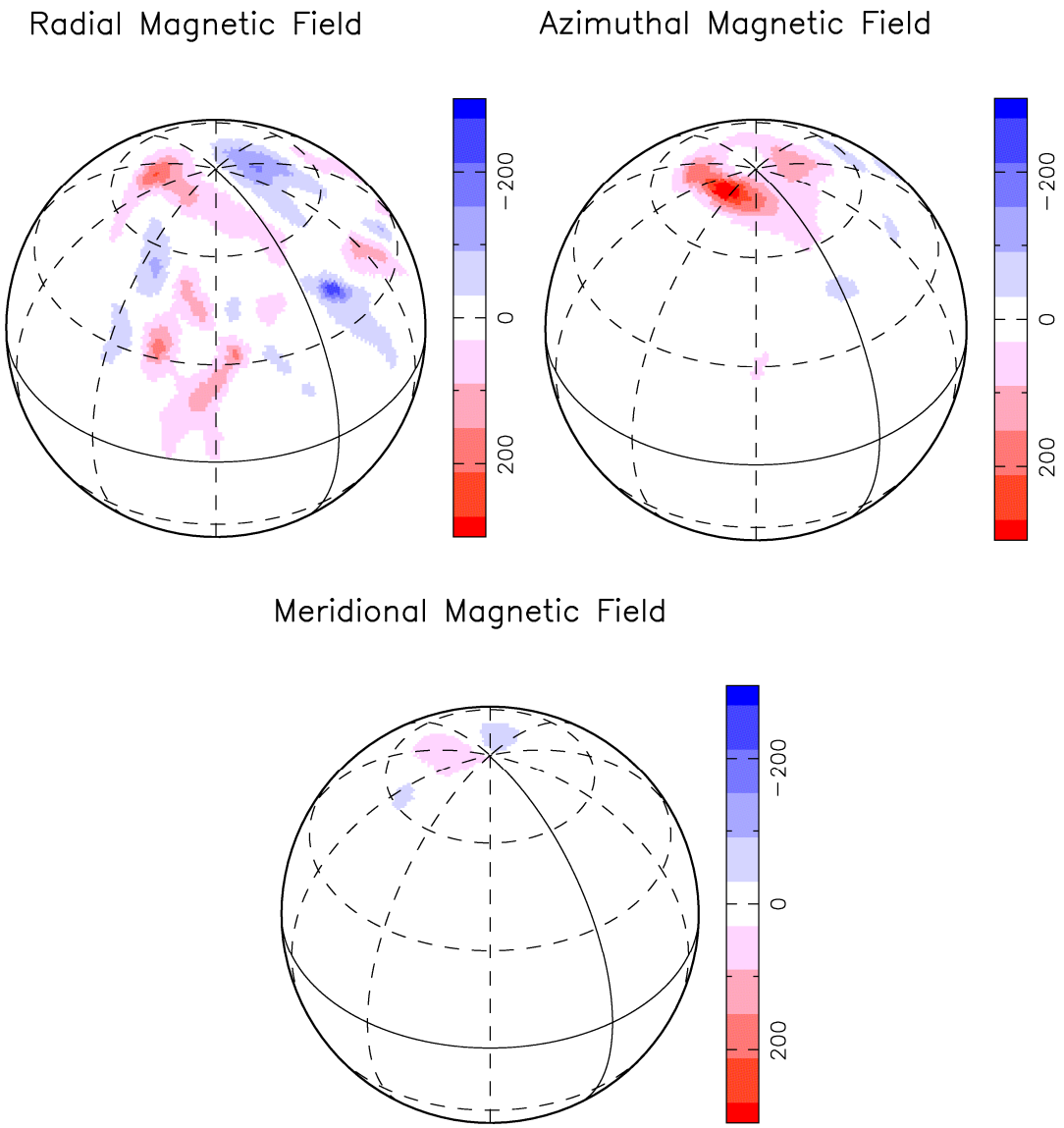

Figure 3.15 Maximum entropy reconstructed magnetic maps of HR 1817. As for Figure 3.14, these are based on all observations across the four nights. However, instead of flattened polar projections, these maps are spherical projections, centred on phase 0.1.

3.4 Results: Differential Rotation of HR 1817

As mentioned in Chapter 1, surface differential rotation can be measured from the rotation of spot features at different latitudes on the stellar surface. However, with HR 1817, due to the weakness of the spot features and the lack of complete phase coverage, an accurate measurement of differential rotation using surface features was inconclusive (Appendix A). Alternately, the same mechanism was applied to the magnetic features on HR 1817, to produce a measurement of the differential rotation of the star. A solar-like differential rotation law is assumed such as that found by Donati et al. (2000) and Donati and Cameron (1997) on other stars which have had differential rotation measured:

$$\Omega(l) = \Omega_{eq} - d\Omega \sin^2 l \qquad (3.2)$$

where $\Omega(l)$ is the rotation rate at latitude l measured in radians d^{-1}, Ω_{eq} is the rotation rate at the equator and $d\Omega$ is the rotational shear between the equator and the pole. By incorporating Equation 3.2 into the imaging process as outlined by Petit et al. (2002), the differential rotation can be measured. Considering Ω_{eq} and $d\Omega$ to be free parameters, the best fit to the data set can be found by a χ^2 minimization method.

This method was applied to the data set produced for Zeeman Doppler Imaging of HR 1817 for various values of Ω_{eq} and $d\Omega$. The χ^2 levels for the various values of the differential rotation are shown in Figure 3.16. Figure 3.17 shows the same data projected out to $\pm 3\ \sigma$. Fitting the derived paraboloid in Figure 3.17 yields values for Ω_{eq} and $d\Omega$ of 6.494 ± 0.010 rad/d and 0.256 ± 0.017 rad/d respectively ($1\ \sigma$ errors). This is equivalent to a rotational period for HR 1817 of ~ 0.98 days. A rotational shear of 0.256 rad/d is very high, and indicates that the equator laps the pole in approximately 23±1.5 days.

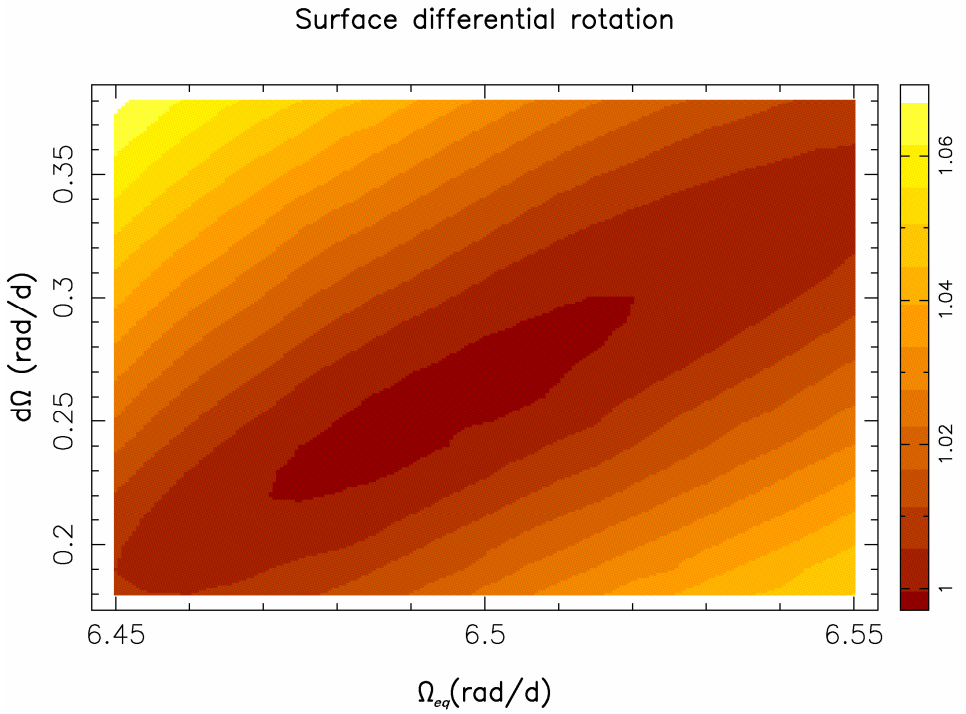

Figure 3.16 Surface differential rotation χ^2 minimization for HR 1817. The plot shows the χ^2 obtained from the maximum-entropy Zeeman Doppler Imaging code. The darker regions correspond to lower χ^2 values.

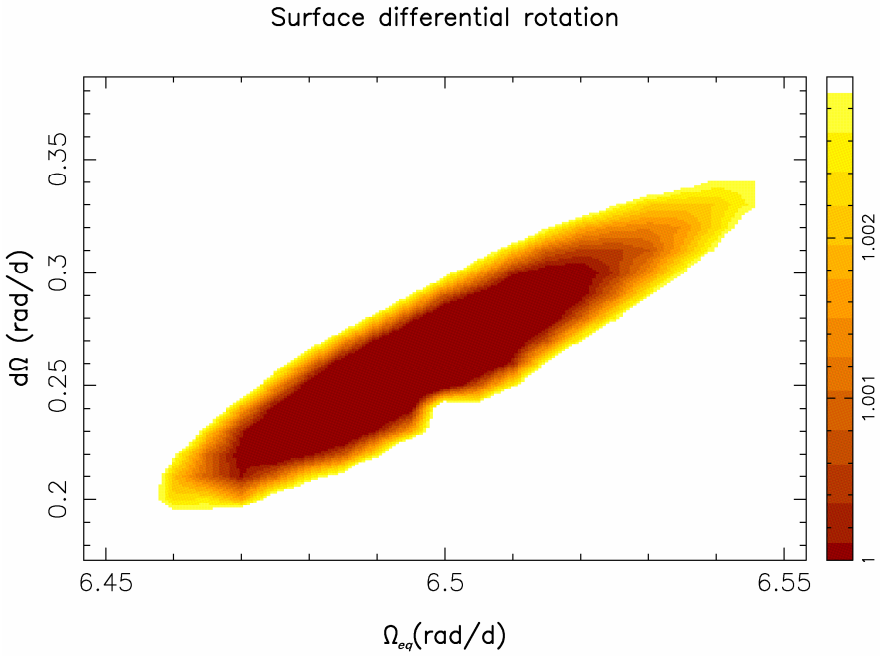

Figure 3.17 Surface differential rotation χ^2 minimization for HR 1817. The plot shows the χ^2 obtained from the maximum-entropy Zeeman Doppler Imaging code. The darker regions correspond to lower χ^2 values. This image corresponds to a projection of $\pm 3\ \sigma$ taken from the data shown in Figure 3.16.

3.5 Measurement of Stellar Inclination and Radial Velocity

When performing the mapping functions in Sections 3.3 and 3.4, it is important to know accurately the stellar inclination and radial velocity of the target star. While the inclination can be calculated as shown in Section 3.2 (Equation 3.1) and the radial velocity can be estimated from the line profiles as shown in Section 3.2, these estimates can be confirmed or refined using a χ^2 minimization method as outlined by Petit et. al. (2002). Taking the line profiles and attempting to generate a map while adjusting the appropriate parameter allows the determination of the minimum χ^2 in each case, thus providing the values used in the mapping processing in Sections 3.3 and 3.4.

Stellar Inclination

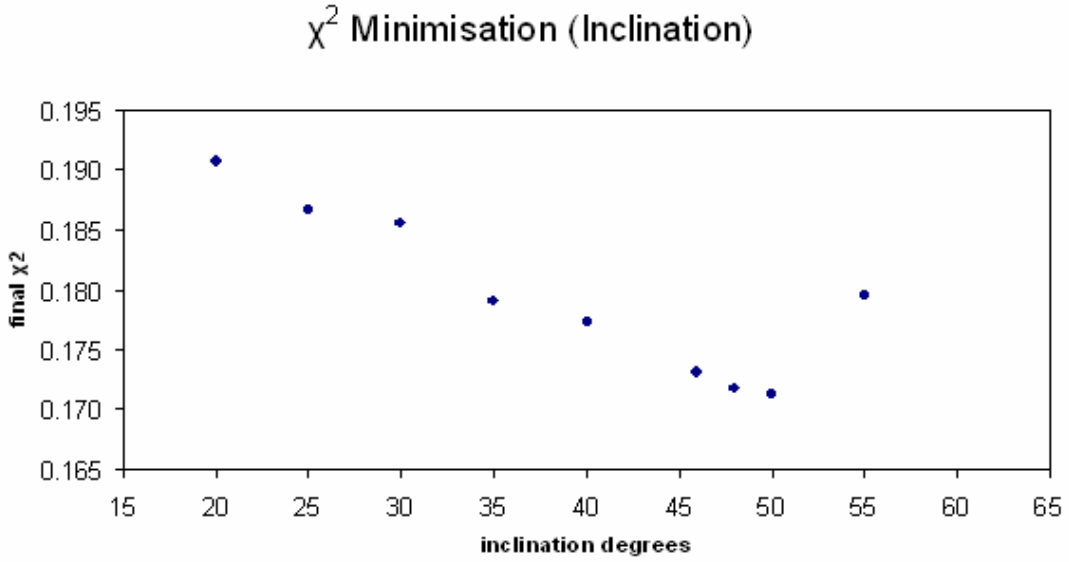

Figure 3.18 χ^2 minimization for the stellar inclination angle. A data point at 45° was excluded as an outlier (replaced by a point at 46°), and at > 55°, the χ^2 is much higher than 0.2 and hence for clarity these values are excluded. The stellar inclination is thus found to be 50°, confirming the earlier calculation in Section 3.2.

As shown in Figure 3.18, the minimum χ^2 is found at a stellar inclination and of 50°. This is the value used in the generation of the maps in earlier sections, and confirms the calculation in Section 3.2.

Radial Velocity

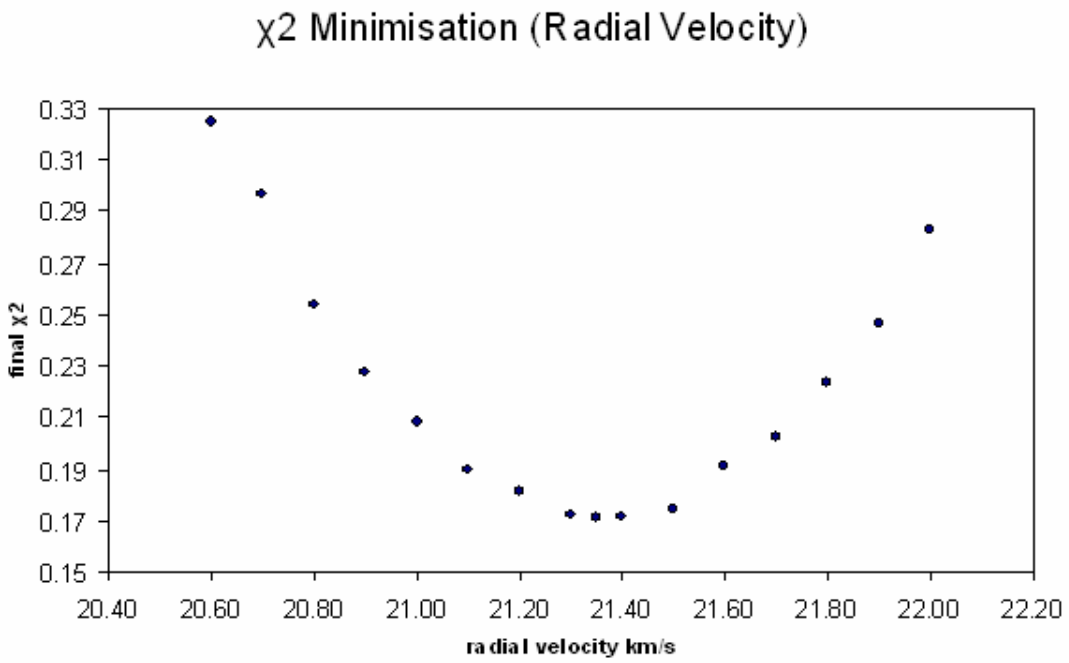

Figure 3.19 χ^2 minimization for the radial velocity of HR1817. The radial velocity is determined to be 21.35 kms^{-1}.

In a similar manner, Figure 3.19 illustrates the χ^2 minimization of the radial velocity. The value of 21.35 kms^{-1} is more accurate than the estimate from the profiles generated in Section 3.1. The value of 21.35 kms^{-1} is used in all of the mapping in Sections 3.2 and 3.3.

3.6 Discussion: HR 1817

In this thesis, I set out to investigate the magnetic activity of the F7 dwarf HR 1817. At the warm end of the continuum of solar-type stars (those stars that have both a radiative

and a convective zone) HR 1817 is an exemplar of how the dynamo processes operate with respect to the depth of the stellar convective zone.

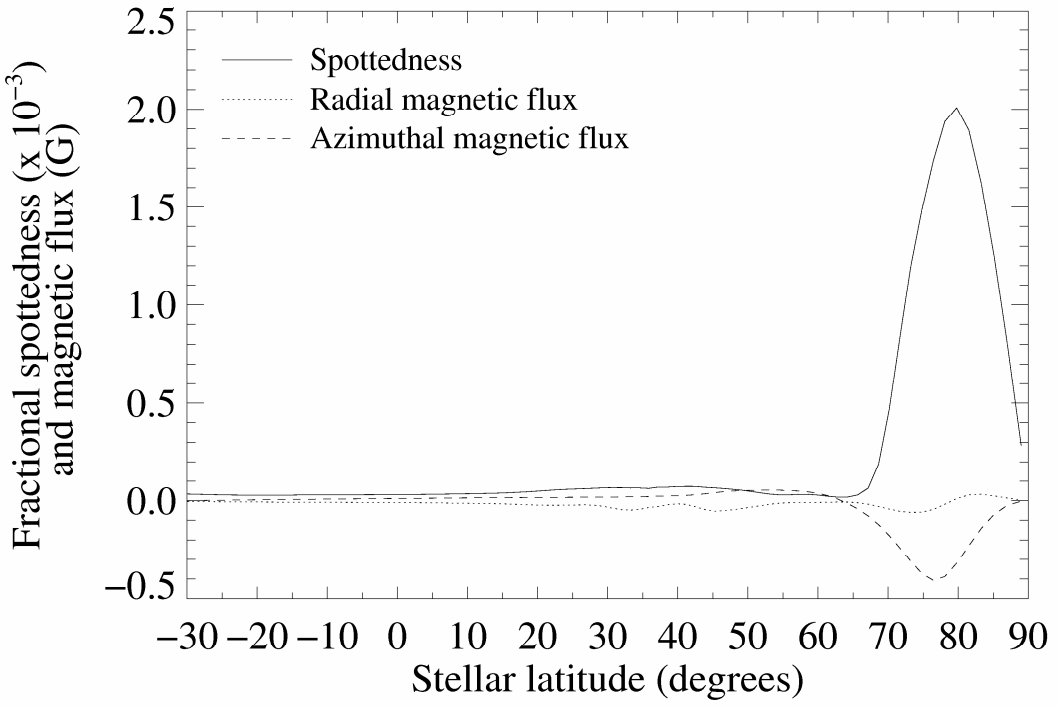

Figure 3.20 Fractional spottedness and fractional magnetic flux versus stellar latitude for HR 1817, based on the average spot occupancy at each latitude as defined by equation 3.3. The solid line represents the fractional spottedness, while the dashed line and dotted line represent the azimuthal field flux and radial field flux respectively.

Spot Coverage

In comparison with G and K dwarf stars investigated with Doppler Imaging previously, HR 1817 exhibits a significantly smaller spot coverage. The one third phase coverage yielded a spot occupancy of only around 2% of the stellar surface. Even given the fact that the relatively small phase coverage of the star means that this is probably an underestimation of the total spot coverage, this is still a significantly lower than the roughly 10% coverage exhibited by other solar-type stars (even if the spot coverage on

HR 1817 were doubled to include a spot at the other pole). Even the ubiquitous polar spot seen in stellar investigations of this type is visibly smaller than that of other solar-type stars which have been Doppler imaged, although the bulk of the spot coverage is disproportionately in the polar spot as shown in Figure 3.20. Fractional spottedness is based on the average spot occupancy at each latitude and is defined by:

$$F(l) = \frac{S(l)\cos(l)dl}{2} \qquad (3.3)$$

where *F(l)* is the fractional spottedness at latitude *l* and *S(l)* is the average spot occupancy at latitude *l*.

The pattern of spot coverage on HR 1817 is also somewhat different to G and K dwarfs previously observed. The surface spot features on HR 1817 (excluding the polar spot) are relatively small, and restricted to the mid-latitudes – between ~ +30° and +60°. They are also not particularly strong features compared to, for example, the polar spot. The fractional spottedness as shown in Figure 3.20 is extremely small at latitudes below +70°. As shown in Figures B.1, B.2, B.3 and B.4, other stars exhibit very large polar spots, extending significantly into lower latitudes, and indeed LQ Hya (K0V) and HR 1099 (K1 subgiant component of an RSCvn system) exhibit significant fractional spottedness all the way to the equator. The paucity of phase coverage on HR 1817 may result in an underestimation of the low-latitude features as the entire path of the spot across the line profile was not observed. This problem is illustrated in Figure 3.9, where very poor phase coverage results in no visible low-latitude features at all.

Although HR 1817 is not a particularly rapid rotator in the context of some of the stars previously investigated using Doppler Imaging, it is still a rapid rotator when compared to the Sun. However, the signficant difference in surface structure seen in

HR 1817 compared to G and K dwarfs cannot be ascribed to rotation. As a warmer star, with a thinner convective zone than other spectral types, I speculate that the difference may be ascribed to differences in the dynamo processes of HR 1817.

Magnetic Topology

Similarly, the magnetic topology of HR 1817 appears quite different to other stars investigated by Zeeman Doppler Imaging. Unlike stars investigated by Donati et al. (2003), HR 1817 does not exhibit a large region of predominantly azimuthal field. In fact, a small ring of azimuthal field is seen in HR 1817, but only near the pole, above +60° latitude. The fractional azimuthal flux shown in Figure 3.20 is neither as broad nor as strong as that shown, for example, by AB Dor (K1V; Figure B.1) or by HR 1099 (Figure B.2). Solanki (2002) proposes that the ring of azimuthal magnetic field around polar spots may be as the result of differential rotation. The observation of the azimuthal ring exhibited by HR 1817, and given its strong differential rotation, is consistent with this speculation. Donati et al. (2003) suggest that the observed large regions of azimuthal field on stars like HR 1099 and AB Dor are evidence of dynamo process distributed through the stellar convective zone. Despite uncertainty in the flux due to incomplete phase coverage, the apparent absence of a large region of azimuthal field on HR 1817, leads me to speculate that it either (a) does not possess or possesses only a weak distributed dynamo process due to its thinner convective zone, and (b) the high rotational shear exhibited by HR 1817 may prevent the formation of magnetic structures within the convective zone. Alternatively the strong rotational shear may simply act to destroy all but the strongest magnetic features before buoyancy brings them to the surface, although

this seems unlikely as strong azimuthal field regions seem to survive over quite long time periods on other stars thus observed which exhibit a high rotational shear (although not as high as HR 1817).

The complex structure of the radial magnetic field on HR 1817 is similarly at variance to that observed on other stars. Despite the richness of the radial field structure, the fractional radial flux (Figure 3.20) shows only small variations from a flat profile. HR 1099 and LQ Hya (Figures B.2 and B.3) show significant variations in the distribution of radial flux. I speculate that the evenness of the fractional radial flux reflects that the structures seen at each latitude are bipolar pairs, and hence the opposite polarities cancel each other cancel each other out (Figure 3.21). I further propose that the small undulations seen in the fractional radial flux plot may also be indicative of slight asymmetry in the latitude of the bipolar pairs produced by Joy's law.

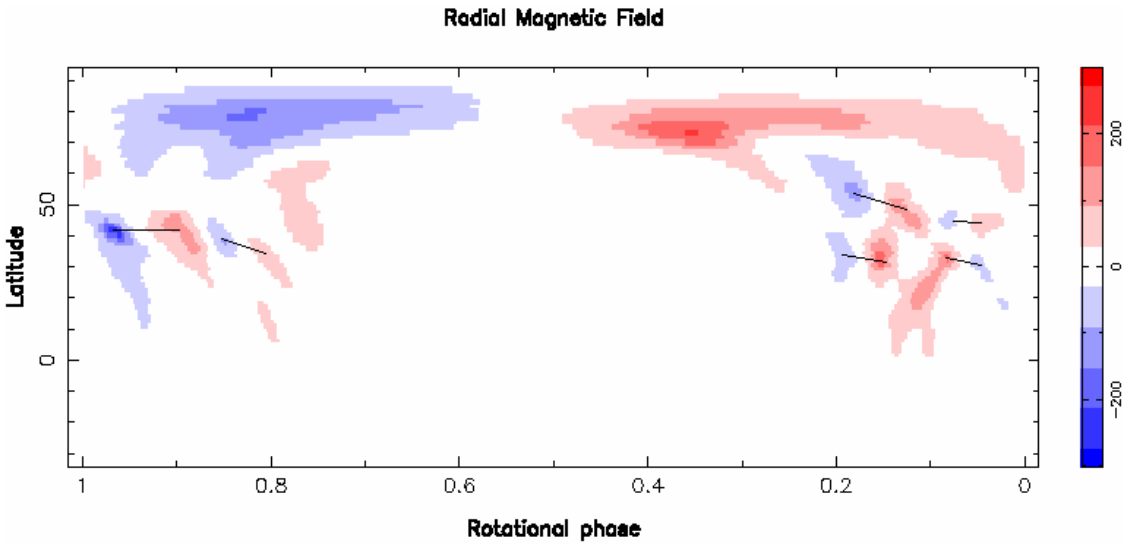

Figure 3.21 Radial magnetic field of HR 1817 (rectangular projection) showing potential bipolar spot areas connected by lines. Note that the spot on the right of each pair is almost invariably slightly lower latitude than the left spot of each pair.

The fact that the observed radial magnetic field produces a complex, asymmetric arrangement of small features, some of which appear to be clearly bipolar leads me to also speculate that there is indeed a dominant interface-layer dynamo at work in HR 1817. Whether this means that there is no distributed dynamo process is unknown.

The significant outstanding difference between HR 1817 and other solar-type stars investigated by ZDI is obviously its spectral type. As a warmer star, the convective zone is thinner than the G and K dwarfs. Whether this is a determining factor in the differences in the operation of the stellar dynamo requires further investigation.

Differential Rotation

HR 1817 has the highest rotational shear of any solar-type star which has had its differential rotation published. The equator laps the pole every ~ 23 days. There appears to be no particular relationship between $d\Omega$ and rotation rate, $d\Omega$ and spectral type (see Table 1.1) or $d\Omega$ and magnetic activity. However, this may simply be as a result of a small sample size. Barnes et al. (2005) demonstrate that there appears to be a broad relationship between temperature and differential rotation (Figure 3.22; adapted from Barnes et al. (2005)). HR 1817 appears to obey this relationship.

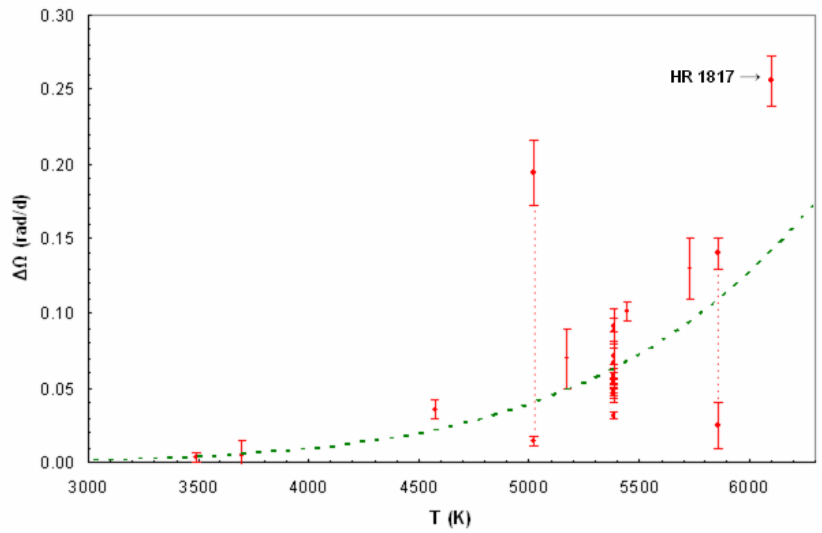

Figure 3.22 Adapted from Barnes et al. (2005) to include HR 1817, a plot of differential rotation ($\Delta\Omega$) versus T_{eff}. There appears to be a relationship between temperature and differential rotation, which HR 1817 obeys. Note that the differential rotation measurement of HR 1817 is that of the magnetic field, whereas the measurements for other stars are obtained using spots.

Having noted broad agreement with this trend, it must be said that HR 1817 exhibits a significantly higher differential rotation than one would necessarily expect from this trend. As has been previously noted, differential rotation has been seen to vary over time. The fact that temporal variations exist may suggest that HR 1817 may have been observed at a time of unusually high differential rotation. More observations of HR 1817 would be required to investigate whether the measurement obtained in 2001-2002 is typical or an extremity. Assuming that like the Sun, the differential rotation is maintained through the convective zone to the radiative zone, one can conclude that the interface layer in HR 1817 is an area of rapid transition from high rotational shear to solid-body rotation. Given that I already speculate that HR 1817 exhibits an interface-layer dynamo, the magnitude of the rotational shear in HR 1817 undoubtedly plays a part in the generation of the magnetic field of HR 1817. However, it is also possible that

there is an opposite, destructive effect on flux bubbles or tubes as they rise though the convective zone, destroying magnetic features before they manifest themselves on the stellar surface.

3.7 In Conclusion

HR 1817 is clearly different to the targets previously imaged using Doppler Imaging and Zeeman Doppler Imaging. Its weak, complex radial magnetic field and its relatively small spot features set it apart from G and K solar-type stars.

The sample size of solar-type stars studied using DI, ZDI and differential rotation analysis is still small. A fuller understanding of dynamo processes in solar-type stars demands an increase in this sample size across spectral types, rotation rates and activity indices.

As far as HR 1817 is concerned, a campaign which provides more comprehensive phase coverage would be desirable to gain a fuller picture of the spot and field topographies. Given the 1-day period of the star, this requires a multi-telescope campaign similar to that conducted by Barnes et al. (2000) for PZ Tel, which also has a period of close to 1 day.

References

Babcock, H.W. 1961. The topology of the Sun's magnetic field and the 22-year cycle. *ApJ*, **133**, 572

Barnes, J.R., Cameron, A. Collier, James, D.J., & Donati, J.-F. 2000. Doppler images from dual-site observations of southern rapidly rotating stars I: Differential rotation on PZ Tel. *MNRAS*, **314**, 162.

Barnes, J.R., Cameron, A. Collier, Donati, J.-F., James, D.J., Marsden, S.C., & Petit, P. 2005 The dependence of differential rotation on temperature and rotation. *MNRAS*, **357**, L1

Baliunas, S. 1991. The past, present and future of solar magnetism: Stellar magnetic activity. *Page 809 of:* Sonnett, C.P., Giampapa, M.S. & Matthews, M.S. (eds), *The Sun in time*. Tucson: The University of Arizona Press.

Brown, S.F., Donati, J.-F., Rees, D.E., & Semel, M. 1991. Zeeman-Doppler imaging of solar-type and Ap stars. IV. Maximum entropy reconstruction of 2D magnetic topologies. *A&A*, **250**, 463.

Budding, E., Carter, B.D., Mengel, M.W., Slee, O.B., & Donati, J.-F. 2002. A radio and optical study of the active young F star HR 1817 (=HD 35850). *PASA*, **19**, 527.

Byrne, P.B. 1996. On the believability of polar spots. *Page 299 of:* Strassmeier, K.G., & Linsky, J.L. (eds), *Stellar surface structure.* Proceedings of the 176th Symposium of the International Astronomical Union, vol. 176. Dordrecht: Kluwer Academic Publishing.

Cameron, A. Collier. 1992. Modeling stellar photospheric spots using spectroscopy. *Page 33 of:* Byrne, P.B., & Mullan, D.J. (eds), *Surface inhomogeneities on late-type stars.* Lecture Notes in Physics, vol 397. Heidelberg, Germany: Springer-Verlag.

Cameron, A. Collier, & Donati, J.-F. 2002. Doin' the twist: secular changes in the surface differential rotation on AB Doradus. *MNRAS*, **329**, L23.

Cameron, A. Collier, Donati, J.-F., & Semel, M. 2002. Stellar differential rotation from direct star-spot tracking. *MNRAS*, **330**, 699.

Carroll, B.W., & Ostlie, D.A. 1996. *An Introduction to Modern Astrophysics*. Reading: Addison Wesley Publishing Company

Carter, B., Brown, S., Donati, J.-F., Rees, D., & Semel, M. 1996. Zeeman Doppler imaging of stars with the AAT. *PASA*, **13**, 150.

Cram, L.E., & Kuhi, L.V. 1989 FGK Stars and T Tauri Stars. Monograph series on nonthermal phenomena in stellar atmospheres. Washington: NASA.

Donati, J.-F. 1999. Magnetic Cycles of HR 1099 and LQ Hydrae. *MNRAS*, **302**, 457.

Donati, J.-F., & Brown, S.F. 1997. Zeeman Doppler imaging of active stars V. Sensitivity of maximum entropy magnetic maps to field orientation. *A&A*, **326**, 1135.

Donati, J.-F., & Cameron, A. Collier. 1997. Differential rotation and magnetic polarity patterns on AB Doradus. *MNRAS*. **291**, 1.

Donati, J.-F., Semel, M., & Praderie, F. 1989. Zeeman Doppler imaging of active stars. II. – Numerical simulation and first observational results. *A&A*, **225**, 467.

Donati, J.-F., Brown, S.F., Semel, M., Rees, D.E., Dempsey, R.C., Matthews, J.M., Henry, G.W., & Hall, D.S., 1992. Photospheric imaging of the RS CVn system HR 1099. *A&A*, **265**, 682.

Donati, J.-F., Semel, M., Carter, B., Rees, D.E., & Cameron, A.C. 1997. Spectropolarimetric observations of active stars. *MNRAS*, **291**, 658.

Donati, J.-F., Cameron, A.C., Hussain, G.A.J., & Semel, M. 1999. Magnetic topology and prominence patterns on AB Doradus. *MNRAS*, **302**, 437.

Donati, J.-F., Mengel, M., Carter, B.D., Marsden, S., Cameron, A. Collier, & Wichmann, R. 2000. Surface differential rotation and prominences of the Lupus post T Tauri star RX J1508.6-4423. *MNRAS*, **316**, 699.

Donati, J.-F., Cameron, A. Collier, Semel, M., Hussain, G.A.J., Petit, P., Carter, B., Mengel, M., Marsden, S.C., Ariste, A. López, & Rees, D.E. 2003a. Dynamo processes and activity cycles of the active stars AB Doradus, LQ Hydrae and HR 1099. *MNRAS*, **345**, 1145.

Donati, J.-F., Cameron, A. Collier, & Petit, P. 2003b. Temporal fluctuations in the differential rotation of cool active stars. *MNRAS*, **345**, 1187.

Gagné, M., Valenti, J.A., Linsky, J.L., Tagliaferri, G., Covino, S., & Güdel, M. 1999. The active corona of HD 35850 (F8V). *ApJ*, **515**, 423.

Granzer, Th., Schüssler, M., Caligari, P., & Strassmeier, K.G. 2000. Distribution of starspots on cool stars. II. Pre-main-sequence and ZAMS stars between 0.4 $M_{\odot}$ and 1.7 $M_{\odot}$. *A&A*, **355**, 1087.

Hussain, G.A.J. 1999. *Magnetic activity in late-type stars*. PhD Thesis, University of St. Andrews, St. Andrews, Scotland.

Jeffers, S.V., Cameron, A. Collier, & Barnes, J.R. 2005. Direct evidence for a polar spot on SV Camelopardalis. *ApJ*, **621**, 425.

Kitchatinov, L.L., & Rüdiger, G. 1995. Differential rotation in solar-type stars: Revisiting the Taylor-number puzzle. *A&A*, **299**, 446.

Kóvári, Zs. 2002. Photometric cycles and starspot tracking on LQ Hya. *Second workshop of young researchers in astronomy and astrophysics, publications of the astronomy department of the Eötvös University*, **12**, 123.

Kurucz, R.L. 1993. *CDROM #13 ATLAS9 atmospheric models) and CDROM #18 (ATLAS9 and SYNTHE routines, spectral line database).*

Marsden, S.C., Waite, I.A., Carter, B.D., & Donati, J.-F. 2004. Doppler imaging of G-dwarfs in two young open clusters. *Astron. Nachr.*, **325**, 246.

Marsden, S.C., Waite, I.A., Carter, B.D., & Donati, J.-F. 2005. Doppler imaging and surface differential rotation of young open cluster stars – I. HD 307938 (R58) in IC 2602. *MNRAS*, **359**, 711.

Marsh, T.R. 1989. The extraction of highly distorted spectra. *PASP*, **101**, 1032.

Mathioudakis, M., & Mullan, D.J. 1999. HR 1817: the EUV properties of an active F dwarf. *A&A*, **342**, 524.

Petit, P., Donati, J.-F., & Cameron, A. Collier. 2002. Differential rotation of cool active stars: The case of intermediate rotators. *MNRAS*, **334**, 374.

Rice, J.B., Wehlau, W.H., Khokhlova, V.L. 1989. Mapping stellar surfaces by Doppler imaging – Technique and application. *A&A*, **208**, 179.

Rüdiger, G., von Rekowski, B., Donahue, R.A., Baliunas, S.L. 1998. Differential rotation and meridional flow for fast-rotating solar-type stars. *ApJ*, **494**, 691.

Saar, S.H. 1988. Improved methods for the measurement and analysis of stellar magnetic fields. *ApJ*, **324**, 441.

Schrijver, C.J. & Zwaan, C. 2000. *Solar and stellar magnetic activity*. Cambridge astrophysics series. Cambridge: Cambridge University Press

Schüssler, M., Caligari, P., Ferriz-Mas, A., Solanki, S.K., & Stix, M. 1996. Distribution of starspots on cool stars. I. Young and main sequence stars of $1M_{\odot}$. *A&A*, **314**, 503.

Semel, M. 1989. Zeeman-Doppler imaging of active stars. I – Basic principles. *A&A*, **225**, 456.

Semel, M., Donati, J.-F., & Rees, D.E. 1993. Zeeman-Doppler imaging of active stars. 3: Instrumental and technical considerations. *A&A*, **278**, 231.

Skilling, J., & Bryan, R.K. 1984. Maximum entropy image reconstruction – General algorithm. *MNRAS*, **211**, 111.

Solanki, S.K. 2002. The magnetic structure of sunspots and starspots. *Astron. Nachr.*, **323** 165.

Strassmeier, K.G., & Rice, J.B. 1998. Doppler imaging of stellar surface structure. VI. HD 129333 = EK Draconis: A stellar analog of the active young Sun. *A&A*, **330**, 685.

Strassmeier, K.G. 2001. Latest results in Doppler imaging. *Page 271 of:* Garcia, R.J., Lopez, R.R., & Osorio, M.R.Z. (eds), *Cool stars, stellar systems, and the Sun. 11th Cambridge workshop.* Astronomical Society of the Pacific Conference Proceedings, vol 223. San Francisco: Astronomical Society of the Pacific.

Tagliaferri, G., Covino, S., Fleming, T.A., Gagné, M., Pallavicini, R., Haardt, F., & Uchida, Y. 1997. Coronal X-ray emission of HD 35850: the ASCA view. *A&A*, **321**, 850.

Thompson, M.J., Christensen-Dalsgaard, J., Miesch, M. S., & Toomre, J. 2003. The Internal Rotation of the Sun. *Annual Review of Astronomy and Astrophysics*., vol. 41**.**, 599

Unruh, Y.C., & Cameron, A. Collier. 1997. Does chromospheric emission mimic polar starspots in Doppler images? *MNRAS*, **290**, L37.

Vogt, S.S., & Penrod, G.D. 1983. Doppler imaging of spotted stars – Application to the RS Canum Venaticorum stars HR 1099. *PASP*, **95**, 565.

Vogt, S.S., Penrod, G.D., & Hatzes, A.P. 1987. Doppler images of rotating stars using maximum entropy image reconstruction. *ApJ*, **321**, 496.

Weber, M., Strassmeier, K.G., & Washuettl, A. 2005. Indications for anti-solar differential rotation of giant stars. *AN*, **326**, 287.

Zuckermann, B., Song, Inseok, Bessell, M.S., & Webb, R.A. 2001. The β Pictoris moving group. *ApJ*, **562**, L87.

Appendix A

Differential Rotation of HR 1817 using Spots

An inconclusive attempt to make a differential rotation measurement of HR 1817 using the spot features rather than the magnetic field was attempted. As shown in Figure A.1, the clear paraboloid shape of the χ^2 minimization is not apparent at the lowest χ^2. Greater phase coverage revealing more features may yield a more definitive result.

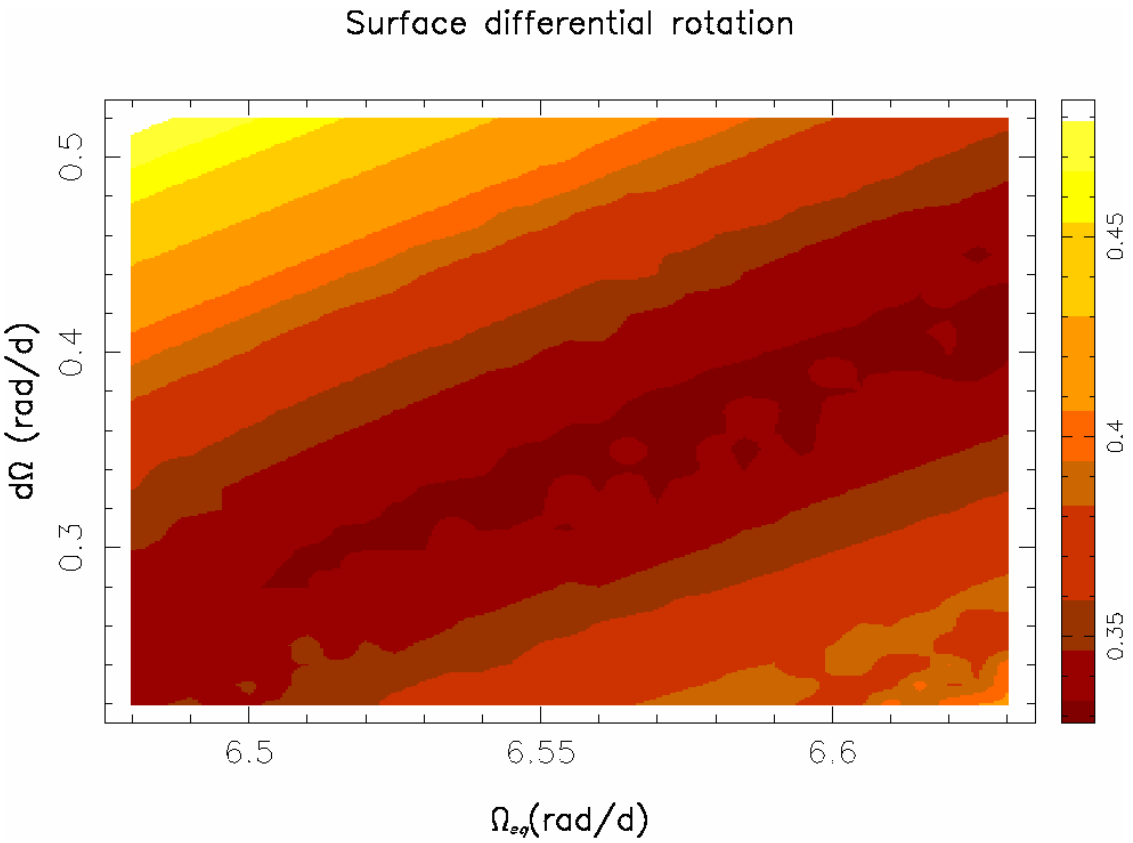

Figure A.1 Surface differential rotation χ^2 minimization for HR 1817 using spots. The plot shows the χ^2 obtained from the maximum-entropy Doppler Imaging code. The darker regions correspond to lower χ^2 values.

Appendix B

Fractional Spottedness of Other Solar-Type Stars

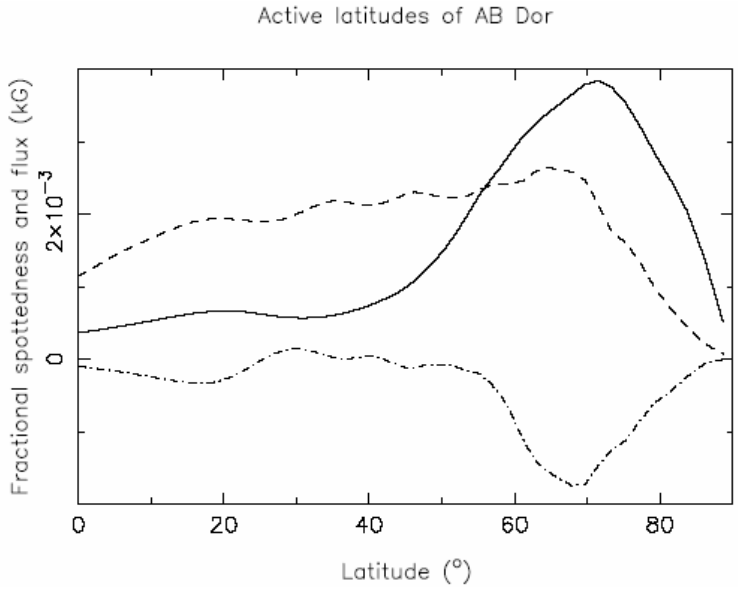

Figure B.1 Fractional spottedness of AB Dor (K0V) from Donati et al. (2003a), showing spottedness (solid line), azimuthal field (dash-dotted line) and quadratic magnetic flux (dashed line – ignores polarity).

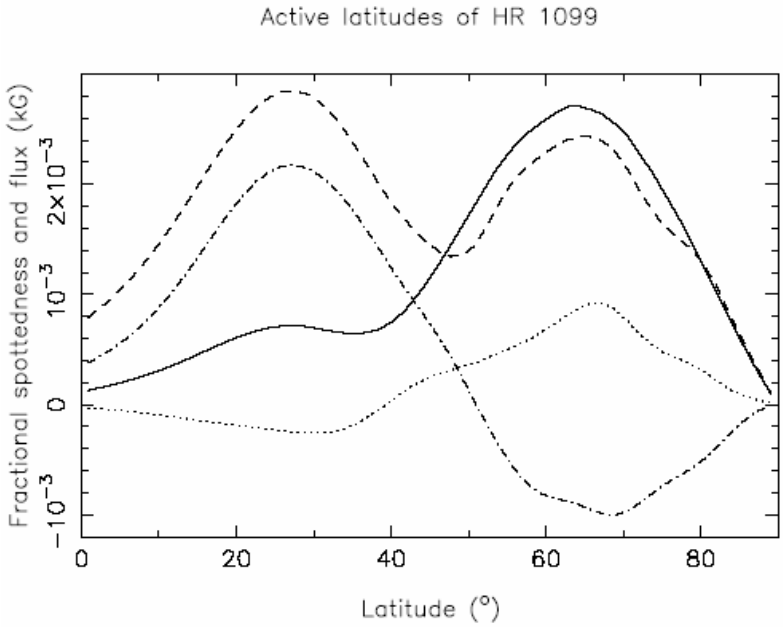

Figure B.2 Fractional spottedness of HR 1099 (K1 subgiant in RSCvn system) from Donati et al. (2003a), showing spottedness (solid line), azimuthal field (dash-dotted line) radial field (dotted line) and quadratic magnetic flux (dashed line – ignores polarity).

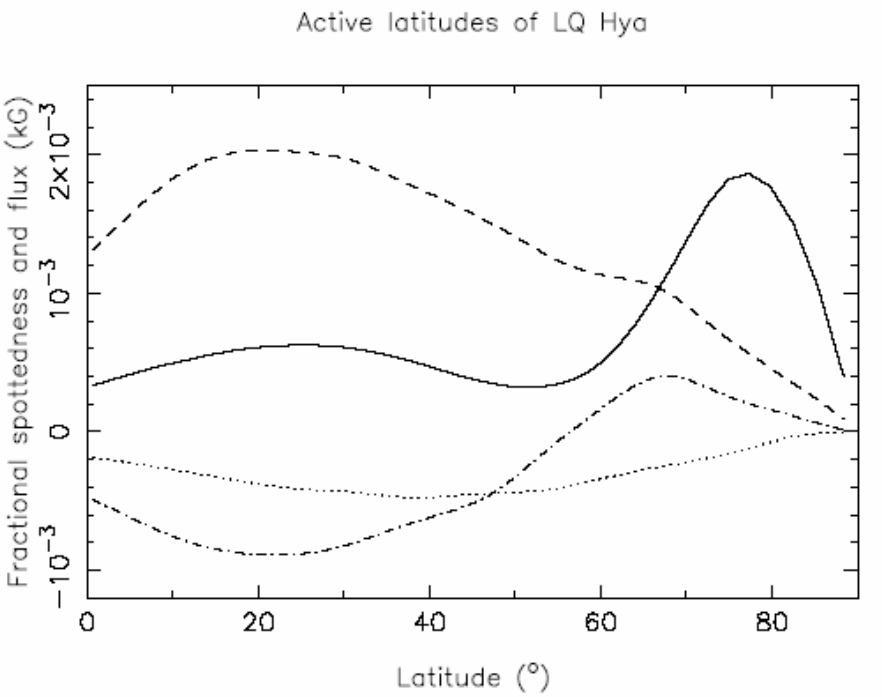

Figure B.3 Fractional spottedness of LQ Hya (K0V) from Donati et al. (2003a), showing spottedness (solid line), azimuthal field (dash-dotted line) radial field (dotted line) and quadratic magnetic flux (dashed line – ignores polarity)..

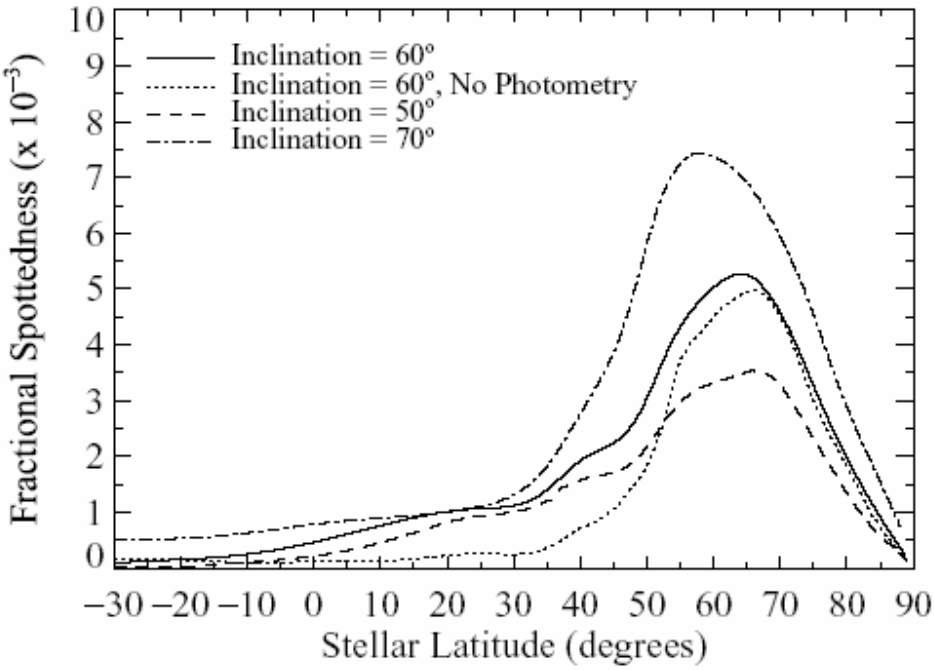

Figure B.4 Fractional spottedness of R58 (G2V) from Marsden et al. (2005), showing spottedness for different inclination angles.